Journal of Environmental Management 401 (2026) 128875

Contents lists available at ScienceDirect

Journal of Environmental Management

journal homepage: www.elsevier.com/locate/jenvman

Research article

Spatiotemporal assessment of wildfire smoke exposure using a low-cost air quality monitoring system in a developing Amazonian city

Domingas de Oliveira Almeida [a,*], Ana Carla dos Santos Gomes [b], Sarah Suely Alves Batalha [c], Tiago Bentes Mandú [d], Fernanda Souza do Nascimento [e], Glauce Vitor da Silva [f], Maria João Costa [g], Ediclê de Souza Fernandes Duarte [g,**]

[a] Postgraduate Program in Natural Resources of the Amazon, Federal University of Western Pará, 68040-255. Santarém, Pará, Brazil
[b] Postgraduate Program in Natural Resources of the Amazon, Institute of Engineering and Geosciences, Federal University of Western Pará, 68040-255. Santarém, Pará, Brazil
[c] Francisco Coimbra Lobato Technical Education School of the State of Pará, 68035-000, Santarém, Pará, Brazil
[d] Federal University of Western Pará, 68040-255. Santarém, Pará, Brazil
[e] Institute of Engineering and Geosciences, Federal University of Western Pará, 68040-255. Santarém, Pará, Brazil
[f] Postgraduate Program in Social Sciences, Institute for Interdisciplinary and Intercultural Studies, Federal University of Western Pará, 68035-110, Santarém, Pará, Brazil
[g] Universidade de Évora, Centro de Investigação em Ciência e Tecnologia para o Sistema Terra e Energia (CREATE), 7000-671, Évora, Portugal

ARTICLE INFO

Keywords:
Atmospheric pollution
Biomass burning
Amazon basin
Early-warning
Air quality network

ABSTRACT

Biomass burning is the dominant source of seasonal air pollution in the Amazon, yet local-scale exposure remains poorly characterized due to sparse monitoring. This study aims to quantify the spatiotemporal dynamics and drivers of $PM_{2.5}$ pollution in Santarém, Brazilian Amazon, by integrating measurements from a dense network of low-cost sensors, satellite-derived fire radiative power (FRP), and reanalysis meteorology throughout 2023. We applied Generalized Estimating Equations (GEE) to evaluate the daily influence of fire activity and meteorological conditions on local $PM_{2.5}$. Mean $PM_{2.5}$ concentrations increased from ~5 μg/m^3 in the rainy season to ~16 μg/m^3 in the dry season, with 94% of exceedances occurring from July–December and a fine-particle dominance ($PM_{2.5}/PM_{10} \approx 0.79$). Peri-urban communities experienced earlier-season pollution peaks, whereas the urban core showed more persistent late-season accumulation. FRP emerged as the primary driver of $PM_{2.5}$, with effect sizes strengthening from 10% (wet season) to 25% (dry season) per standard deviation, while meteorological factors such as wind speed and boundary-layer height played secondary but modulating roles. A negligible weekend–weekday contrast confirmed that smoke overwhelmingly dominates over local traffic emissions. Finally, we operationalized these relationships into a low-computational-cost FRP–Meteo–$PM_{2.5}$ polar radar tool for identifying high-risk smoke transport corridors. These results provide actionable evidence for early warning and highlight the urgent need for targeted fire management to reduce public health risks in developing Amazonian cities.

1. Introduction

Air pollution is widely recognized as one of the main causes of worldwide morbidity and mortality as well as increasing respiratory and cardiovascular diseases and premature mortality (Requia et al., 2021; Ye et al., 2022; de Souza Fernandes Duarte et al., 2023; de Souza Fernandes Duarte et al., 2024, 2025; Monteiro dos Santos et al., 2024) especially of low-income populations (Alahmad et al., 2023; Lelieveld et al., 2020; Rentschler and Leonova, 2023; Tran et al., 2023). The inhalable PM_{10} (aerodynamic diameter ≤10 μm) and $PM_{2.5}$ (aerodynamic diameter ≤2.5 μm) air particles have received attention due to their ability to penetrate deep into the respiratory system, causing serious harm to human health (Pozzer et al., 2023; Huang et al., 2025). It is estimated that 94% of the global population is exposed to unsafe levels of $PM_{2.5}$ concentrations (Rentschler and Leonova, 2023).

Among the health impacts, both short- and long-term exposures to PM_{10} and $PM_{2.5}$, the most notable are the worsening of respiratory diseases, such as asthma and chronic obstructive pulmonary disease

* Corresponding author.
** Corresponding author.
E-mail addresses: 99domingas@gmail.com (D. de Oliveira Almeida), edicle.duarte@uevora.pt (E. de Souza Fernandes Duarte).

https://doi.org/10.1016/j.jenvman.2026.128875
Received 16 October 2025; Received in revised form 14 November 2025; Accepted 2 February 2026
Available online 13 February 2026

(COPD), and the increased susceptibility to respiratory infections in vulnerable patients (Hoffmann et al., 2022; Maung et al., 2022; Song et al., 2023). Furthermore, the International Agency for Research on Cancer (IARC) has classified $PM_{2.5}$ and PM_{10} particles as carcinogenic to humans due to their association with an increased risk of lung cancer (Tsai et al., 2022). Because of the increasing evidence of air pollution impacts on human health, the World Health Organization (WHO) updated its global air quality guidelines in 2021, substantially reducing the recommended limits. The annual mean exposure limit for $PM_{2.5}$ was lowered from 10 μg/m^3 to 5 μg/m^3, and for PM_{10} from 20 μg/m^3 to 15 μg/m^3. The corresponding 24-h mean limits are now 15 μg/m^3 for $PM_{2.5}$ and 45 μg/m^3 for PM_{10} (World Health Organization, 2021).

A primary source of these particulates on a continental scale in South America is biomass burning (Artaxo et al., 2005; Freitas et al., 2005; Koengkan et al., 2021; Valente and Laurini, 2023; Libonati et al., 2021). Each year, the convergence of dry weather, available biomass, and ignition sources in ecosystems like the Cerrado and Amazon lead to hundreds to thousands of wildfires, which in turn release vast amounts of carbonaceous aerosols and trace gases during the dry season (Moritz et al., 2005; Hoelzemann et al., 2009; Libonati et al., 2021). While urban industrial emissions dominate near large cities, biomass burning from deforestation and wildfires constitutes a major regional source. These emissions are not confined locally since under favorable meteorological conditions, smoke plumes can be injected high into the atmosphere, allowing their impact to extend far beyond the fire sources (Artaxo et al., 2005; Freitas et al., 2005; Monteiro dos Santos et al., 2024; de Souza Fernandes Duarte et al., 2021).

Consequently, South America biomass burning is a major source of atmospheric pollutants, with emissions that possess a significant transboundary dimension. These wildfires release substantial quantities of primary pollutants, including particulate matter ($PM_{2.5}$, PM_{10}), black carbon, carbon monoxide (CO), methane (CH_4), and nitrogen oxides (NO_x) (Urbanski et al., 2008). Furthermore, these emissions contribute to the formation of secondary pollutants such as ozone (O_3) and polycyclic aromatic hydrocarbons through atmospheric reactions (Jaffe and Wigder, 2012; Singh and Tripathi, 2021; Koengkan et al., 2021). Recent analyses also show significant warming trends and an intensification of temperature extremes across Brazil (de Souza et al., 2025), conditions that can exacerbate drought severity, promote fire ignition, and enhance smoke accumulation.

In the Amazon region, wildfires are predominantly anthropogenic, driven by agribusiness expansion and land-use change (Libonati et al., 2021; Valente and Laurini, 2023), an important gap persists regarding local-scale exposure within Amazonian urban centers. The region's naturally high humidity typically inhibits ignition, making natural fires rare (Libonati et al., 2021; INPE, 2021). However, the annual dry season (June to December) creates conditions conducive to fire, a situation exacerbated by drought-intensifying climate patterns like El Niño (Johnston et al., 2012; Souza et al., 2020). The impacts of these fires cascade across scales. Globally and regionally, biomass burning in the Amazon is the main source of $PM_{2.5}$—a complex mixture of organic and inorganic compounds—and other aerosols that are transported thousands of kilometers by atmospheric currents, influencing climate and air quality far beyond their sources (Freitas et al., 2005; Reddington et al., 2015). Consequently, extensive research has focused on this long-range transport and its impact on major urban centers in southeastern Brazil, such as São Paulo and Rio de Janeiro (Freitas et al., 2005; de Fatima Andrade et al., 2015; de Almeida Albuquerque et al., 2018; de Souza Fernandes Duarte et al., 2021; Martins et al., 2018; Deroubaix et al., 2024; Santos et al., 2024; Pereira et al., 2021; Squizzato et al., 2021).

While air pollution in Brazil's major urban centers is dominated by traffic and industrial sources (Sant'Anna et al., 2020; Pereira and Limongi, 2015), the Amazon faces a distinct crisis where the seasonal fire regime superimposes a decisive pollution load. However, a critical gap persists in quantifying local-scale impacts; the transboundary footprint of fires is well-documented, but far fewer studies examine the immediate consequences for cities within the basin, largely due to sparse ground monitoring (Vormittag et al., 2021). In Santarém, for example, residents face a dual exposure: (i) regional advection of biomass-burning $PM_{2.5}$, which recurrently drives concentrations to levels exceeding WHO guidelines by a factor of five during the dry season (Sant'Anna et al., 2021), and (ii) locally generated pollution from civil construction, traffic, agriculture, and land-clearing burns (Cardoso et al., 2020). These local sources are intertwined with traditional and agro-industrial activities, producing a layered, under-characterized air-quality burden. The stakes of this exposure are high, as toxicological and epidemiological evidence links smoke-borne particulates to DNA damage, lung cell death (Alves et al., 2017), and adverse birth outcomes (Silva et al., 2014), placing communities at the core of the burning biome at significant risk.

At the population scale, wildfire smoke was estimated to contribute to ~5000 premature deaths in Brazil in 2019 (Nawaz and Henze, 2020). These impacts are amplified when heat extremes and drought co-occur with fires, conditions that both intensify burning and heighten health vulnerability (Sutanto et al., 2020; Vitolo et al., 2019). Temperature extremes—now increasing in frequency across Brazil (de Souza et al., 2025)—represent an additional compounding stressor that heightens vulnerability to smoke exposure. Regional analyses further show that drought-enhanced fire seasons correspond to spikes in respiratory hospitalizations in Amazon region (Machado-Silva et al., 2020), and recent modeling for the Amazon basin indicates large and predictable health burdens attributable to wildfire smoke (de Souza Tadano et al., 2024). Together, this evidence argues for expanding high-resolution monitoring and source-aware analyses in smaller Amazonian cities, where communities face a dual burden from transported smoke plumes and local emissions such as traffic, construction dust, refuse/land-clearing burns and industries (Cardoso et al., 2020). Importantly, coordinated actions to curb deforestation-related fires and urban emissions could reduce PM concentrations by up to ~30% in the dry season (Reddington et al., 2015), yielding immediate public-health benefits.

Conventional air-quality monitoring relies on reference-grade stationary analyzers, which are accurate but expensive for dense spatial deployment, particularly in remote regions like the Brazilian Amazon (Kumar et al., 2014). To address this, low-cost sensor (LCS) networks have emerged as a viable complementary tool. When deployed following established best practices—including initial co-location for calibration, rigorous quality control, and corrections for humidity interference—these networks provide dense, near-real-time data important for understanding pollution dynamics in developing urban areas (de Souza et al., 2017; Morawska et al., 2018; Penza, 2020). Recent studies demonstrate the potential of LCS devices for urban monitoring and calibration improvement (Blaga and Gautam, 2024). Appropriately calibrated, LCS networks can resolve fine spatial and temporal gradients in particulate matter filling critical gaps in exposure assessment for smaller Amazonian cities (Silva et al., 2021).

Interpreting LCS data, however, requires concurrent meteorological information, as weather strongly modulates particulate concentrations. Key controlling factors include wind speed and direction, governing pollutant advection and source alignment; planetary boundary-layer height, controlling vertical dilution; and precipitation, which removes particles via wet scavenging (Liu et al., 2024; Zender-Swiercz et al., 2024). The Amazonian context presents specific challenges: persistently high relative humidity promotes hygroscopic growth of fine particles, artificially increasing measured $PM_{2.5}$ mass (Martin et al., 2010; Pöhlker et al., 2016), while rain events can lead to rapid clearing (Andreae et al., 2015; Wang et al., 2016). Conversely, warm, dry spells during the burning season favor the accumulation of smoke (Artaxo et al., 2013; Reddington et al., 2015). Temperature further influences aerosol composition through processes like gas-particle partitioning of semi-volatile organics (Robinson et al., 2007). Critically, periods of atmospheric stagnation—characterized by low winds and a shallow boundary layer—consistently correlate with elevated particulate

concentrations and documented respiratory health risks in the region (Ignotti et al., 2010; Oliveira et al., 2012).

In this context, this work provides a city-scale, physics-aware assessment of biomass burning impacts on air quality in Santarém, a medium-sized city in the Brazilian Amazon, over the 2023 calendar year. We employed an integrated data-modeling approach, fusing observations from a dense network of low-cost sensors measuring air pollutants concentrations and meteorological variables across urban and peri-urban zones with daily satellite-derived fire hotspot and European Center for Medium-Range Weather Forecasts (ECMWF) ERA5 reanalysis data. After quality control, including winsorization and standardization, it was constructed as a daily site-level panel dataset. After this, the dataset was modeled using Generalized Estimating Equations (GEE) with a Gamma log-link model, which effectively accounts for the right-skewed distribution of $PM_{2.5}$ and the temporal correlation of repeated measurements. A key innovation is the use of distance-explicit fire radiative power (FRP) metrics that capture spatial and temporal decay of fire influence.

The contribution of this work is twofold: first, it delivers novel, quantitative, and seasonally resolved estimates of how fire activity and meteorology drive local air pollutant concentrations in an under-monitored yet highly exposed Amazonian urban context, directly addressing a key knowledge gap. Second, it operationalizes these statistical relationships into a practical, low-computational-cost early-warning system. This tool synthesizes community sensor data, near-real-time fire activity, and ERA5 meteorological fields to visually identify upwind fire corridors and assess short-term transport risk. The entire methodology is designed to be replicable in other developing Amazonian cities and communities where conventional air quality monitoring and forecasting infrastructure is scarce.

2. Methods

2.1. Study area

Santarém municipality (Fig. 1) is located at 2°24′52″ S and 54°42′36″ W, in the state of Pará, right in the central portion of the Brazilian Amazon rainforest. It covers a territorial area of 17,898.39 km^2 and has an estimated population of 360,871 inhabitants (IBGE, 2022). The Santarém microregion comprises eight municipalities—Alenquer, Belterra, Curuá, Mojuí dos Campos, Monte Alegre, Placas, and Prainha—with Santarém serving as the principal economic and political hub (SEDOP, 2017). Situated at the confluence of the Tapajós and Amazon rivers, Santarém is the third most populous city in Pará and the main urban center in the western Amazon, particularly in terms of commerce and services. It plays a central role in the so-called Lower Tapajós River Basin, which spans the states of Amazonas (3%), Pará (38%), and Mato Grosso (59%) and encompasses a drainage area of approximately 500, 000 km^2 (IBGE, 2022).

The climate of Santarém, according to the Köppen–Geiger classification updated by Peel et al. (2007), corresponds to a typical tropical monsoon regime (*Am*). The rainy season extends from January to June, with mean monthly precipitation reaching ~400 mm. In contrast, the dry season occurs from August to November, when rainfall does not usually exceed 100 mm per month. July and December are considered transitional months between these two seasonal extremes. The mean annual temperature in the region is approximately 26 °C, with an average relative humidity of about 80% and a total annual precipitation of around 2000 mm (INMET, 2022).

The study sites are distributed across urban and peri-urban areas, comprising a total of 19 monitoring stations from the research project *"Pilot Network for Innovation in Air Quality Monitoring in the Western Region of Pará: Guardians of the Air"*. In the urban area of Santarém, twelve (12) stations (red dots) are distributed across eight (08) major residential neighborhoods, while four (04) additional stations are located in the communities of Caranazal and Maracanã. In this sector, approximately 40% of the public space remains covered by native vegetation, whereas only about 8% of the territory is urbanized (Fig. 1). The remaining seven (07) stations (blue dots) are situated in four (04) peri-urban communities (Ramal dos Coelhos, Alter do Chão, and Cucurunã), located between 3 km and 30 km from the urban center of Santarém (Table 1). This peri-urban zone represents the "green belt" of the metropolitan region, a transitional landscape where urban and rural environments converge, composed of forests, wetlands, secondary vegetation, and patches of the so-called Amazonian rainforest. Among these, Alter do Chão stands out due to its historical, economic, social, cultural, and environmental significance, being recognized as the most important peri-urban tourist district of Santarém, with a population of approximately 5000 inhabitants (IBGE, 2022; SEBRAE, 2003).

2.2. In-situ data collection and processing

Air temperature (°C), relative humidity (%), $PM_{2.5}$ (μg/m^3), and PM_{10} (μg/m^3) were monitored daily throughout 2023 at 19 sites (Fig. 1). For particulate matter, we employed the low-cost optical sensor SDS011, which has been largely used and validated in air quality monitoring studies (Genikomsakis et al., 2018; Wardoyo et al., 2020; Božilov et al., 2022; Sakila et al., 2023; Alonso-Pérez and López-Solano, 2023;

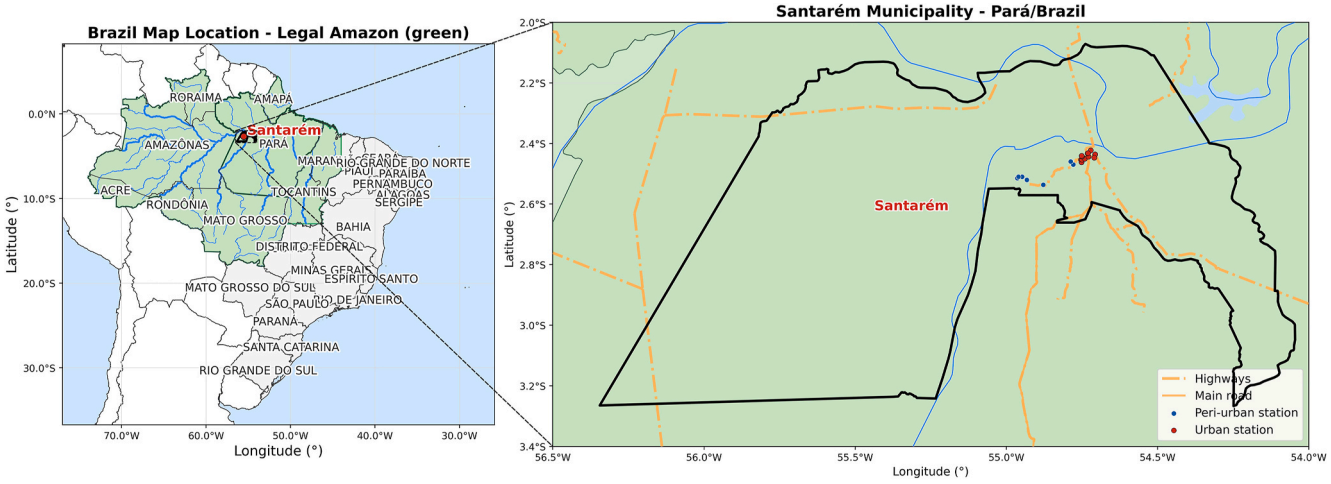

Fig. 1. Brazil's Legal Amazon region showing forest (green), rivers and lakes are drawn in blue; state boundaries in black. Santarém municipality (PA) is outlined in red and labeled. In the left is the regional view of Brazil's Legal Amazon region; in the right is Santarém municipality with location of air-quality monitoring stations, with Urban sites in red and Peri-urban sites in blue.

Table 1
Study sites for air quality of the research project "Pilot Network for Innovation in Air Quality Monitoring in the Western Region of Pará: Guardians of the Air".

ID	Stations in the Urban Area (Residential neighborhoods of Santarém municipality)	ID	Stations in the Peri-urban Area (Communities of the SMR)
U-01	Caranazal	PU-01	Ramal dos Coelhos
U-02	Jardim Santarém	PU-02	São Pedro
U-03	Alvorada	PU-03	Alter do Chão 1
U-08	Maracanã	PU-04	Alter do Chão 2
U-04	São Cristovão	PU-05	Cucurunã
U-05	Caranazal 1	PU-06	Alter do Chão 3
U-06	Amparo	PU-07	Alter do Chão 4
U-07	Santíssimo		
U-12	Maracanã 1		
U-09	Santarenzinho		
U-10	Aldeia		
U-11	Diamantino		

Almeida et al., 2023, 2025; Martins et al., 2024). The SDS011 is designed for both indoor and outdoor measurements of $PM_{2.5}$ and PM_{10}. Its operation is based on light scattering: a laser beam irradiates the sampled air, dust particles scatter the light, and a photodiode detects the scattered intensity. The microcontroller then converts the signal into $PM_{2.5}$ and PM_{10} concentrations. According to the manufacturer, the sensor resolution is 0.3 μm, with an accuracy of ±15% (minimum ±10 $\mu g/m^3$), and a measurement range from 0 to 1000 $\mu g/m^3$.

Temperature and relative humidity were measured using a DHT22 (AM2302) sensor, which has been extensively validated in environmental monitoring applications (Lita et al., 2016; Priya et al., 2017). The DHT22 has an operating range of −40 to 80 °C (±0.5 °C accuracy) and 0–100% RH (±2% accuracy). All sensors were integrated into a microcontroller-based acquisition platform (Arduino Uno), enabling automated data collection, processing, and storage. The use of Arduino coupled with low-cost sensors for meteorological and atmospheric monitoring has been successfully demonstrated in previous studies (Al Ahasan et al., 2018; Andrade et al., 2024; Kelechi et al., 2022; Listyarini et al., 2021; Mullick et al., 2024).

Measurements of PM_{10}, $PM_{2.5}$, relative humidity (%), and air temperature (°C) were collected every 5 min, operating near-continuously from 1 January to December 31, 2023. Data quality control included removal of spurious values (e.g., $PM_{2.5} = 999.9\ \mu g/m^3$), checks for timestamp integrity (duplicates, gaps, and clock shifts), and application of calibration corrections. We also performed cross-site screening by comparing simultaneous measurements among nearby sensors to identify outliers or drift. After QC, data was aggregated to hourly, daily, and monthly means. For validation of climatological behavior, we verified that average PM concentrations followed the expected seasonal pattern—lower during the rainy season (January–June) and higher during the dry season (July–December). Subsequent analyses classified records by study location (urban vs. peri-urban) and by season.

2.3. Satellite-derived fire data

Daily fire activity data over the study area were obtained from NASA/NOAA's *Fire Information for Resource Management System* (FIRMS: https://firms.modaps.eosdis.nasa.gov/), which provides global active fire data derived from the Moderate Resolution Imaging Spectroradiometer (MODIS) sensors onboard the Terra and Aqua satellites, as well as from the Visible Infrared Imaging Radiometer Suite (VIIRS) instruments aboard the Suomi-NPP, NOAA-20, and NOAA-21 platforms (Justice et al., 2002; Giglio et al., 2003; Giglio et al., 2016; NASA, 2023). The MODIS Collection 6.1 Fire and Thermal Anomalies product (MCD14DL) detects active fires and thermal anomalies at a spatial resolution of approximately 1 km and a temporal resolution of one day. Fire detections are represented as point locations corresponding to the center of the 1 km pixel where the thermal anomaly is identified by the contextual fire detection algorithm (Giglio et al., 2003). These data were downloaded directly from FIRMS (NASA, 2023). After download, the fire data was pre-processed to the Amazon region (5°N–14°S, 74°W–42°W). The procedure ensures that only fire detections within the geographic boundaries of the Amazon basin relevant to this study were retained, while maintaining the original FIRMS data structure for consistency and reproducibility.

2.4. ERA5 reanalysis data

Meteorological data were obtained from the ERA5 reanalysis, produced by the European Centre for Medium-Range Weather Forecasts (ECMWF) through the Copernicus Climate Data Store (CDS) (Hersbach et al., 2020). ERA5 provides global atmospheric reanalysis fields at a horizontal resolution of 0.25° × 0.25° (~25 km at the equator) and hourly temporal resolution. The dataset used was *ERA5 single levels reanalysis* at hourly temporal resolution for the year 2023, covering the Amazon region (5°N, 74°W, 14°S, 42°W). The variables retrieved included 10 m zonal and meridional wind components (u10, v10), 2 m temperature (t2m), 2 m dewpoint temperature (d2m), total precipitation (tp), and boundary layer height (blh).

For each monitoring station in the Santarém network, the nearest ERA5 grid point was extracted. From the primary variables, additional diagnostics were derived, including 10 m wind speed and wind direction, 2 m air temperature in °C, 2 m relative humidity calculated using the Magnus formula, and total precipitation converted to millimeters. Hourly series were aggregated into daily datasets: mean values were computed for wind speed, air temperature, relative humidity, and boundary layer height, while precipitation was accumulated as daily totals. Wind direction was averaged using a circular mean to account for its directional nature. The final outputs consisted of station-based hourly and daily meteorological time series for subsequent analysis.

2.5. Statistical modeling of air pollution-fire-meteorological variables

To understand how weather patterns influence pollutant concentrations, we modeled the joint relationship among daily $PM_{2.5}$, fire activity and meteorological conditions using a longitudinal framework that accounts for dependence across repeated observations within sites. When data are collected repeatedly over time and/or across clustered locations, correlation among observations can bias standard errors if ignored. We therefore used Generalized Estimating Equations (GEE) a semi-parametric approach that provides consistent regression estimates and heteroscedasticity-consistent (HC) standard errors under mild assumptions (Liang and Zeger, 1986; Zeger and Liang, 1986; Hardin and Hilbe, 2013). GEE estimates are asymptotically normal, enabling hypothesis tests for main effects and interactions (Ananth and Preisser, 1999).

We constructed a site–day panel for 2023 by merging, for each monitoring site ("local") and calendar date, daily $PM_{2.5}$ (outcome), 2-m air temperature (°C), and relative humidity (%) from the *Cuidadores do Ar* network with fire radiative power (FRP) metrics derived from FIRMS/MODIS and, when available, daily ERA5 covariates (10-m wind speed, boundary-layer height, precipitation and its 1-day lag). ERA5

temperature and humidity were intentionally excluded to avoid duplicating the network's measurements. FRP exposure around each site was quantified in three complementary ways: (i) distance-limited sums within circular buffers of 25, 50, 75, and 100 km, (ii) a proximity-weighted composite that emphasizes nearby sources

$$FRP_{it}^{combo} = 1.00 \times FRP_{it}^{25} + 0.5 \times FRP_{it}^{50} + 0.25 \times FRP_{it}^{100} \quad (1)$$

and (iii) an exponential distance-decay index

$$FRP_{it}^{(\delta)} = \sum_{j} FRP_{ij}\, exp\left(-d_{ij} / \delta\right) \quad (2)$$

with decay scales $\delta \in \{30, 50, 70\}$ km that reflect physically plausible attenuation of influence with distance. To capture short-term carryover, 1- and 2-day lags of the composite and decay-based FRP indices were generated. Records without detected fires were set to zero for FRP features, while occasional gaps in optional meteorological covariates were imputed using site-specific medians. Prior to modeling, all continuous predictors were made robust to extremes via winsorization at the 1st and 99th percentiles and then standardized to z-scores to facilitate coefficient comparability.

Temperature effects were modeled nonlinearly—using a natural cubic spline (user-specified degrees of freedom)—because temperature can influence $PM_{2.5}$ through multiple thresholded processes (boundary-layer mixing, secondary aerosol formation, and fire behavior), and exploratory diagnostics suggested departures from linearity. In contrast, relative humidity was entered linearly since, over the observed range, its association with $PM_{2.5}$ was approximately monotonic and strongly correlated with precipitation and boundary-layer height; a linear term preserves parsimony and limits collinearity. To evaluate moisture-dependent fire impacts, we additionally included an interaction between standardized FRP and standardized relative humidity, allowing the FRP effect on $PM_{2.5}$ to vary across humidity conditions. This processing produced a harmonized, analysis-ready dataset in which exposure, meteorology, and outcome are temporally aligned at the daily scale and comparable across sites.

Because daily $PM_{2.5}$ is strictly positive and right-skewed, we modeled its conditional mean with a generalized linear model using a Gamma family with a log link, embedded in a longitudinal GEE framework to account for correlation within sites over time. Let Y_{it} denote daily $PM_{2.5}$ for site i on day t and

$$\mu_{it} = E[Y_{it} \vee x_{it}] \quad (3)$$

The mean model is:

$$log\{\mu_{it}\} = \beta_0 + \beta_{FRP} Z_{it}^{FRP} + \beta_T^{\top} B_T(T_{it}) + \beta_{RH} Z(RH_{it}) + \beta_{it}\left[Z_{it}^{FRP} . Z(RH_{it})\right] + \beta_{met}^{\top} Z_{it}^{met} \quad (4)$$

where Z_{it}^{FRP} contains the standardized FRP metrics selected for a given specification (e.g., buffer sums, exponential distance-decay indices, and short lags), $B_T(T_{it})$ represents temperature either via a natural cubic spline basis (user-defined degrees of freedom) or an orthogonalized quadratic form, $Z(RH_{it})$ is standardized relative humidity, and Z_{it}^{met} includes optional standardized meteorological controls. All continuous covariates are winsorized (1st–99th percentiles) and then z-scored, so each coefficient corresponds to a one–standard deviation change in the predictor. The Gamma variance is

$$Var(Y_{it} \vee x_{it}) = \phi \mu_{it}^2 \quad (5)$$

with dispersion $\phi > 0$, consistent with heteroscedasticity increasing with the mean for $PM_{2.5}$.

Estimation proceeds via Generalized Estimating Equations (Liang and Zeger, 1986), which solve:

$$\sum_{i=1}^{m} D_i^T V_i^{-1} (y_i - \mu_i) = 0 \quad (6)$$

$$V_i = A_i^{1/2} R(\alpha) A_i^{1/2} \quad (7)$$

Here, sites i define clusters and days t provide the within-cluster ordering; $D_i = \partial \mu_i / \partial \beta^{\top}$; A_i is diagonal with entries $\phi \mu_{it}^2$; and $R(\alpha)$ is a working correlation.To reflect plausible temporal dependence, we compare AR(1) correlation $[R]_{ts} = \rho^{t-s \vee}$ with an exchangeable structure $[R]_{ts} = \rho$ for $t \neq s$; if the primary fit fails to converge, the model automatically falls back to the exchangeable form. Inference uses the robust (sandwich) covariance, yielding asymptotically normal estimates and valid standard errors under mild misspecification of R (.) (Liang and Zeger, 1986; Hardin and Hilbe, 2013).

Because the link is logarithmic, coefficients admit a multiplicative interpretation: for a standardized predictor x_k , $exp(\beta_k)$ is the effect multiplier on the mean $PM_{2.5}$ for a one-SD increase in x_k; equivalently, the percent change is $(exp\{\beta_k\} - 1) \times 100$. Confidence intervals for multiplicative effects are obtained by exponentiating the coefficient intervals. To examine hydrometeorological regime dependence, the model is fit separately for the wet (Jan–Jun) and dry (Jul–Dec) seasons; we then contrast seasonal sensitivities on the log-effect scale. Collinearity is assessed via the predictor correlation matrix and variance inflation factors (VIF) computed on the final design matrix. Among competing FRP specifications (buffer radii, decay scales, lag structures) and correlation structures, model adequacy and parsimony are compared using QIC (Quasi-likelihood under the Independence model Criterion; Pan, 2001) when available, with full coefficient tables, robust standard errors, z-statistics, p-values, and 95% confidence intervals reported for transparency.

This study's contribution is a physics-aware, longitudinal framework that links near-surface $PM_{2.5}$ to satellite-derived fire activity and local meteorology. Instead of treating fire simply as counts in an arbitrary window, we construct distance-explicit FRP exposures—multi-radius buffer sums and exponential distance-decay indices with short lags—-that approximate how influence should diminish with source–receptor separation and time. Effects are estimated with a Gamma–log GEE aligned with the positive, right-skewed distribution of daily $PM_{2.5}$ and accounting for serial correlation and site clustering, yielding multiplicative effect estimates (percent changes per one-SD increase). The model captures nonlinear temperature responses (splines), humidity-modulated fire impacts (FRP × RH interaction), and seasonal stratification (wet vs. dry), revealing regime-dependent sensitivities characteristic of the Amazon. Preprocessing (winsorization, standardization), explicit collinearity diagnostics (correlation matrices, VIF), and QIC-based specification comparison enhance stability, transparency, and reproducibility.

The final objective of this work is to provide a low-cost, near-real-time early-warning system that fuses community $PM_{2.5}$ observations (Project: *Guardians of the Air*), 1-km MODIS active-fire detections (FIRMS/MCD14DL), and ERA5 10-m wind speed/direction to generate daily FRP–Wind–$PM_{2.5}$ polar radar maps for Santarém and surroundings. This tool is designed to run with modest computational resources and without the need for complex chemical-transport models, providing actionable situational awareness for communities in the central Amazon with limited infrastructure. Fig. 2 provides a working diagram of the entire low-cost air quality monitoring and modeling framework developed for Santarém, Brazilian Amazon, summarizing the data sources, preprocessing steps, construction of the site–day panel, statistical modeling workflow, and the final early-warning application.

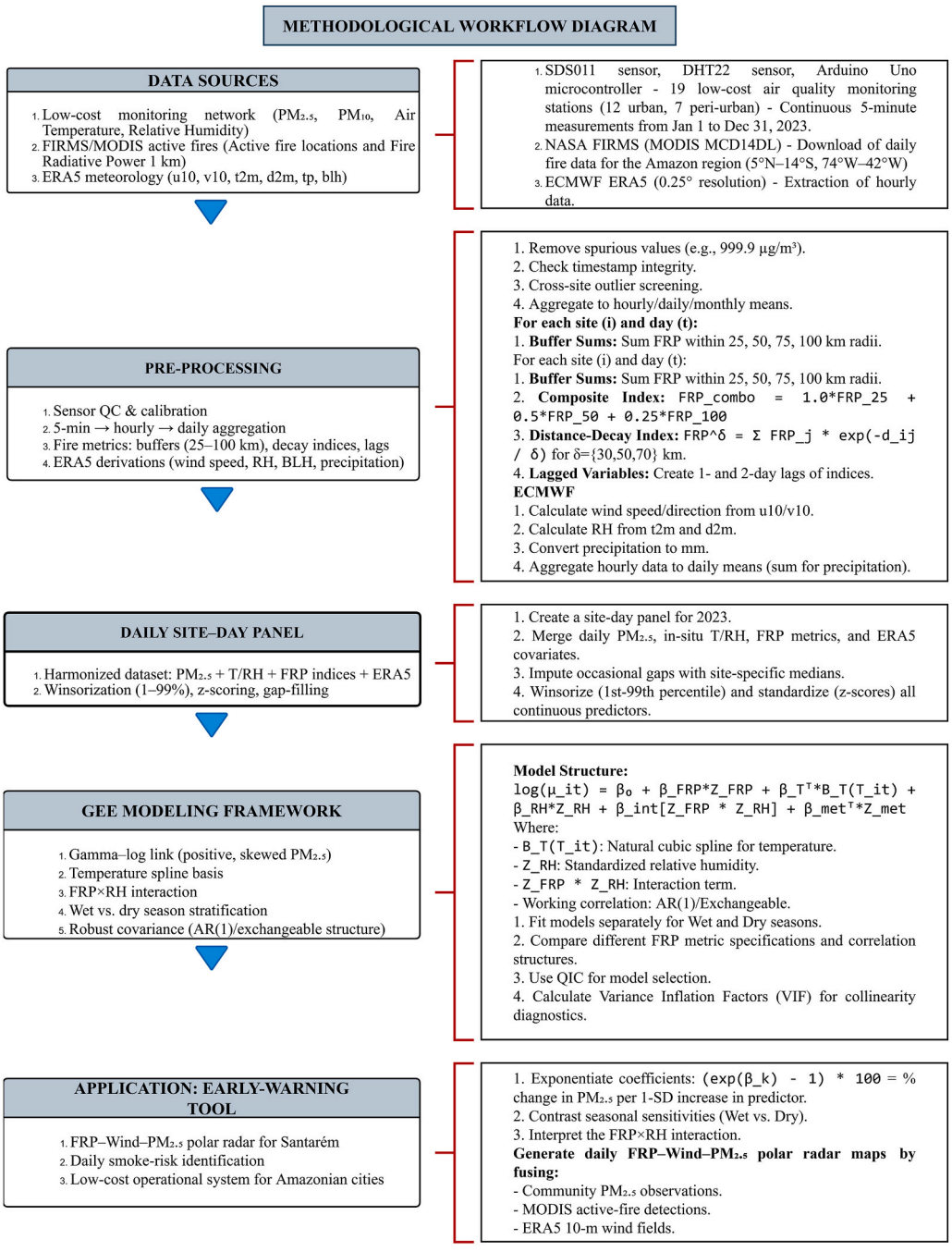

Fig. 2. Working diagram of the low-cost air quality monitoring and modeling framework for Santarém, Brazilian Amazon.

3. Results

3.1. Evaluation of environmental data

Fig. 3(a and b) summarizes daily particulate dynamics across Santarém city in 2023. Average $PM_{2.5}$ and PM_{10} remain low with few peaks and stable during the rainy season (Dec–May), then rise sharply from June through November with frequent exceedances of the WHO 24-h guidelines (15 µg/m^3 for $PM_{2.5}$; 45 µg/m^3 for PM_{10}). Variability widens markedly in the dry/fire season, indicating strong spatial heterogeneity as smoke plumes episodically impact different parts of the city. Peri-urban stations exhibit earlier and larger spikes than urban stations. The fine-to-coarse composition (Fig. 3(c and d)) co-evolves with seasonality: the $PM_{2.5}/PM_{10}$ ratio, a proxy for particle size composition, hovers at lower values in the wet months—indicating a larger coarse-mode contribution—and then increase toward 0.7–0.9 in Sep–Nov, signaling fine-particle dominance typical of biomass-burning smoke. Lower ratios in the rainy season suggest stronger coarse-mode contributions. Together, Fig. 3(a–d) shows a strong seasonal control on air quality, with the dry-season fire regime driving both higher concentrations and finer particle composition and revealing marked spatial heterogeneity between urban and peri-urban environments.

Fig. 4(a and b) show daily Standardized daily anomalies (z-scores) within each group for temperature (red), relative humidity (blue), $PM_{2.5}$ (red dashed), and PM_{10} (black) for Urban and Peri-urban stations. Positive (negative) values indicate above- (below-) average conditions for that group. During the rainy season (Jan–Jun), temperature anomalies stay mostly negative to near-zero while humidity is modestly positive,

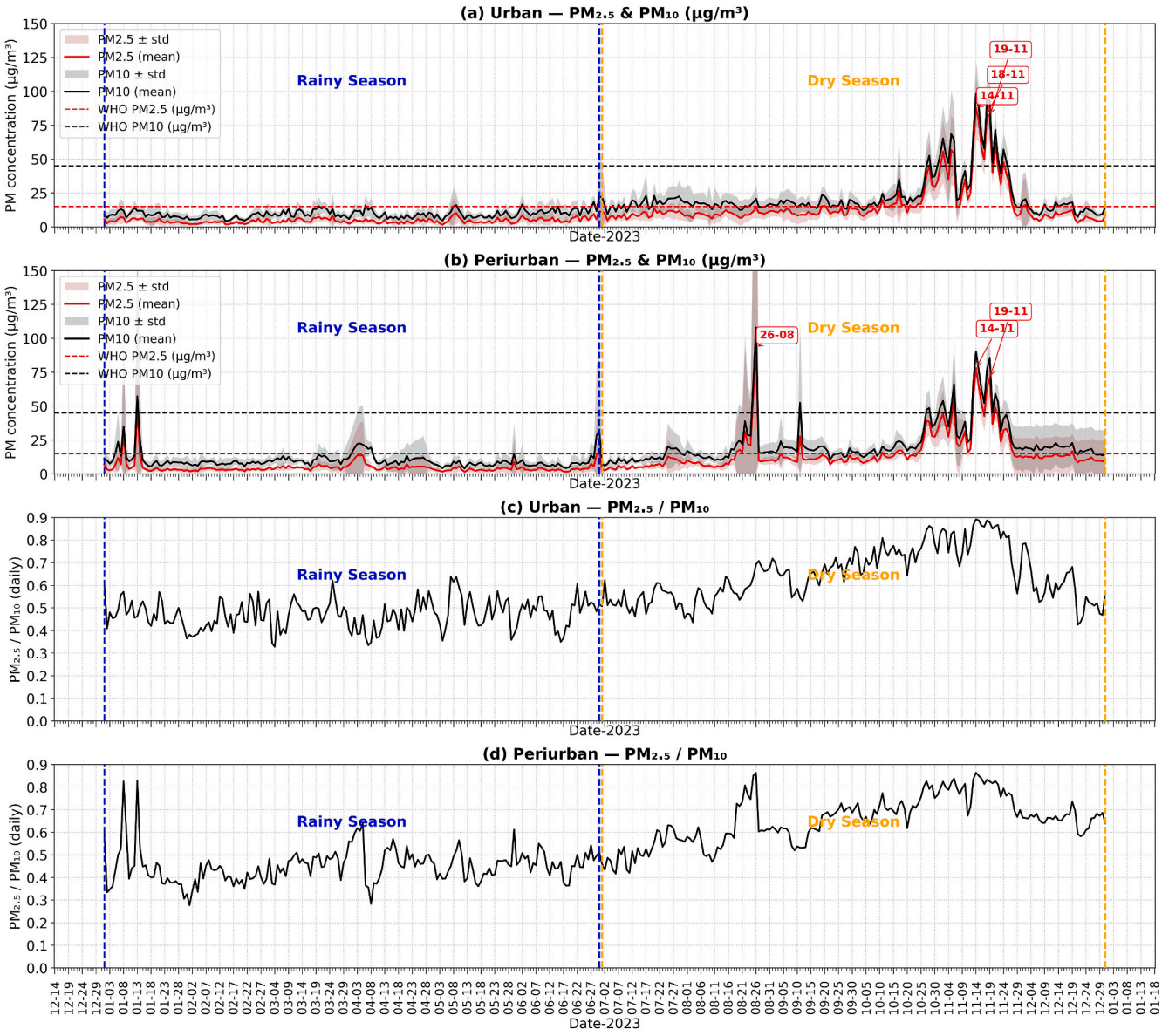

Fig. 3. Daily particulate-matter dynamics in Santarém for the year of 2023 from the low-cost sensor network: **(a–b)** Area-averaged $PM_{2·5}$ (red) and PM_{10} (black) with standard deviation envelopes across stations in each group (Urban, Peri-urban). Horizontal dashed lines show the WHO 24-h guideline values ($PM_{2·5}$ = 15 µg/m^3; PM_{10} = 45 µg/m^3); **(c–d)** Daily $PM_{2·5}$/PM_{10} ratio for Urban and Peri-urban groups. The blue dashed line marks the rainy season (Jan–Jun) and the orange dashed line marks the dry/fire season (Jul–Dec).

and particulate anomalies hover near zero—consistent with efficient wet scavenging and deeper boundary layers that keep concentrations low. From July onward (dry/fire season) the state change: temperature anomalies become persistently positive and humidity negative, and both $PM_{2·5}$ and PM_{10} anomalies increase, with sharp smoke episodes in September–November. The co-evolution of higher temperature, low relative humidity and high particulate matter concentration is the canonical meteorological signature of smoke-impacted days in tropical dry seasons.

Urban versus peri-urban behaviour differs in timing and magnitude. Peri-urban sites show an earlier onset of positive PM anomalies (late August/early September) and stronger excursions ($PM_{2.5}$ up to ~+5–6 σ, PM_{10} up to ~+4–5 σ), together with deeper negative RH anomalies (≈−3 σ to −4 σ). Urban sites peak later (October–November) and with higher amplitude, suggesting closer distance from fire smoke corridors. Across both groups, $PM_{2·5}$ tracks PM_{10} but with larger standardized deviations, indicating a fine-particle–dominated aerosol during smoke events. Across both groups, $PM_{2·5}$ generally departs more strongly than PM_{10}, indicating a fine-particle-dominated aerosol during smoke events. The synchronized pattern—higher temperature, lower humidity, higher PM—is the canonical meteorological signature of smoke-impacted days in the central Amazon dry season.

Table 2 shows the average daily mean concentrations of $PM_{2·5}$ and PM_{10} (µg/m^3) and 2-m air temperature (°C) and relative humidity (%) for urban (n = 12) and peri-urban (n = 7) sub-networks in Santarém during 2023. Across the year, daily $PM_{2·5}$ ranged from 1.55 µg/m^3 (rainy season, peri-urban) to 107.72 µg/m^3 (dry season, peri-urban), while PM_{10} ranged from 4.05 to 124.52 µg/m^3 over the same periods. Seasonal contrasts dominate the signal: in the peri-urban area, mean (±SD) $PM_{2·5}$ increased from 5.05 ± 5.06 µg/m^3 (Jan–Jun) to 16.23 ± 15.22 µg/m^3 (Jul–Dec), and PM_{10} from 10.55 ± 6.59 to 23.37 ± 17.24 µg/m^3. The urban area shows a similar pattern, with $PM_{2·5}$ rising from 4.42 ± 1.63 to 16.27 ± 15.37 µg/m^3 and PM_{10} from 9.23 ± 2.77 to 22.78 ± 16.39 µg/m^3 between the rainy and dry seasons, respectively. Inter-area differences are modest relative to the seasonal gradient—their means and dispersions largely overlap—although peri-urban maxima

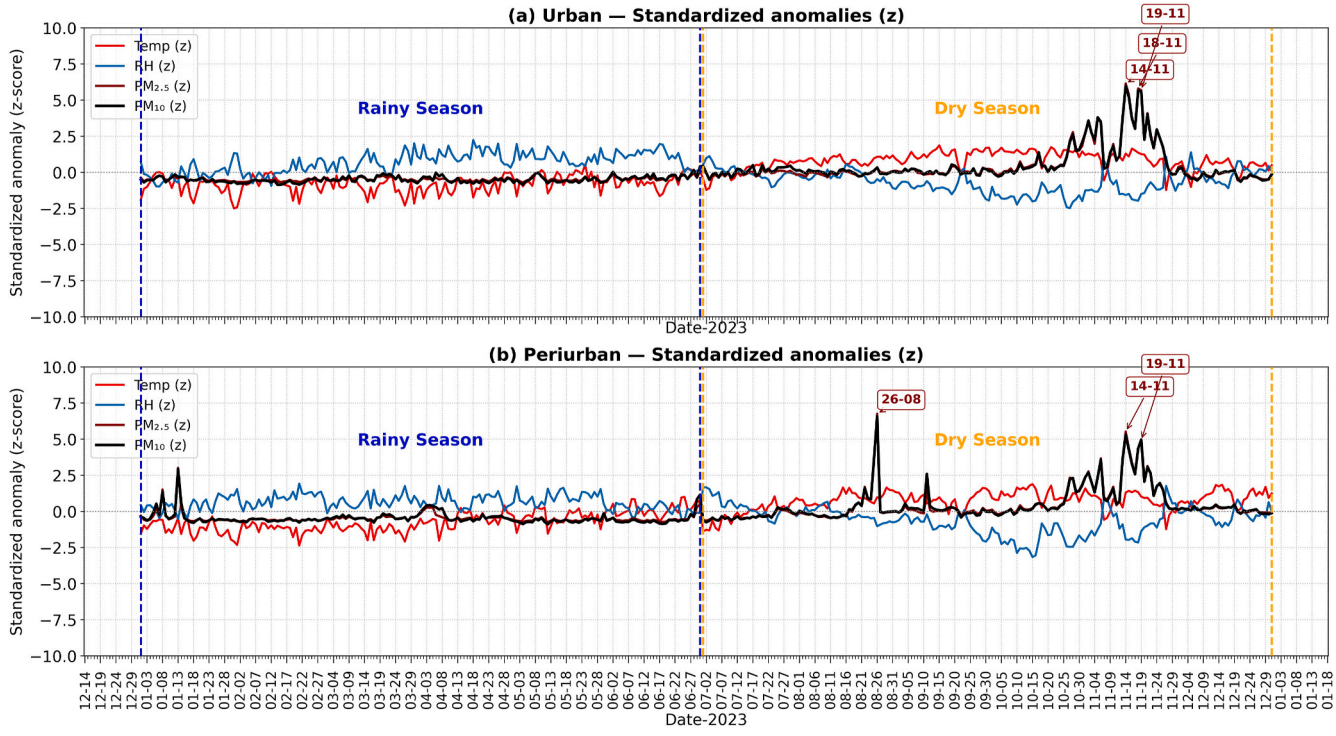

Fig. 4. Standardized daily anomalies (z) of meteorology and PM for the year of 2023: **(a)** Urban and **(b)** Peri-urban stations. Lines: air temperature, solid red; relative humidity, solid blue; $PM_{2.5}$, red dashed; PM_{10}, black dashed. The horizontal zero line marks the climatological mean. Background shading highlights the rainy season (Jan–Jun; light blue) and dry season (Jul–Dec; light tan).

Table 2
General characteristics of air quality in the study area during 2023.

Atmospheric parameters	$PM_{2.5}$ (μg/m^3)				PM_{10} (μg/m^3)				Temperature (°C)				Relative humidity (%)			
Seasonal Period	Rainy season		Dry season		Rainy season		Dry season		Rainy season		Dry season		Rainy season		Dry season	
Study zone	Peri-urban	Urban	Peri-urban	Urban	Peri-urban	Urban	Peri-urban	Urban	Peri-urban	Urban	Peri-urban	Urban	Peri-urban	Urban	Peri-urban	Urban
Average value	5.05	4.42	16.23	16.27	10.55	9.23	23.37	22.78	30.21	30.9	32.71	33.51	78.43	75.15	71.67	67.26
Standard deviation	5.06	1.63	15.22	15.37	6.59	2.77	17.24	16.39	1.27	0.96	1.15	1.01	3.10	4.07	6.09	4.44
Minimum value	1.55	1.63	2.58	3.10	4.05	4.52	6.01	7.09	27.32	28.24	29.39	29.94	71.60	65.49	55.32	56.8
25% of the values	2.98	3.30	8.73	8.68	7.45	7.25	14.78	14.76	29.31	30.43	32.12	33.03	76.26	71.96	67.45	64.37
Median	3.95	4.06	11.49	10.62	9.06	8.68	18.42	17.13	30.04	31.01	32.87	33.67	78.40	75.58	72.78	67.29
75% of the values	5.40	5.53	15.34	15.05	11.05	11.33	22.71	21.48	31.17	31.56	33.53	34.26	80.51	78.19	75.84	70.54
Maximum value	54.77	10.65	107.72	86.76	65.29	20.66	124.52	97.10	33.24	32.71	34.94	35.08	86.42	83.74	86.13	78.54

are higher, consistent with greater exposure to upwind fire corridors. As expected, dry-season temperatures are higher and relative humidity lower than in the rainy season in both settings (see Table 2). Notably, the urban dry-season mean $PM_{2.5}$ (16.27 μg/m^3) slightly exceeds the WHO 24-h guideline of 15 μg/m^3, similar to the peri-urban average (16.23 μg/m^3) which also exceeds this limit; seasonal PM_{10} means remain well below the 45 μg/m^3 guideline.

Table S1 shows that guideline exceedances are overwhelmingly a dry-season phenomenon. For $PM_{2.5}$ (WHO 24-h guideline = 15 μg/m^3), there were 977 exceedances in the dry season versus 60 in the rainy season—94% of all 2023 exceedances (977/1037) occurred from July–December. For PM_{10} (WHO 24-h guideline = μg/m^3), 394 exceedances occurred in the dry season compared with 17 in the rainy season—96% of all exceedances (394/411). Thus, exceedances are ~16 × ($PM_{2.5}$) and ~23 × (PM_{10}) more frequent in the dry period, underscoring the seasonal escalation of health risk.

Table S2 reports monthly means of the $PM_{2.5}/PM_{10}$ ratio by season. During the rainy season (Jan–Jun) the ratio is nearly steady at 0.45–0.48, indicating a larger coarse-mode contribution consistent with wet scavenging and fewer smoke intrusions. With the onset of the dry season (Jul–Dec) the ratio increases from 0.53 (Jul) to a peak of ~0.79 (Nov), then relaxes to 0.58 (Dec)—a clear shift toward fine-particle dominance typical of biomass-burning episodes. The pattern shows that the transition to a fine-dominated aerosol is widespread across the network rather than driven by a few sites. These results reinforce that the most hazardous fraction ($PM_{2.5}$) becomes proportionally larger during the fire season, aligning with the exceedance counts.

Table S3 presents the daily mean concentrations of $PM_{2.5}$ and PM_{10}

(μg/m^3), categorized by monitoring station, area (Urban/Peri-urban), season (Rainy: Jan–Jun; Dry: Jul–Dec), and day type (Weekdays: Mon–Fri; Weekend: Sat–Sun). Analysis reveals a modest and site-specific weekend effect, which is negligible compared to the pronounced dry-to-wet seasonal signal. In urban stations, weekend concentrations for both PM fractions are generally slightly higher (~1–3 μg/m^3, often within one standard deviation), as seen at Alvorada and Maracanã. This increment is more consistent for PM_{10}, suggesting contributions from coarse particle resuspension due to leisure traffic. However, the trend is not universal, with sites like Diamantino showing higher weekday levels, indicating the persistent influence of routine work-week activity.

The pattern is more distinct in certain peri-urban areas (Table S3). Locations with recreational focus, notably Alter do Chão 1, show clear weekend elevations during the dry season, coupled with high variability—pointing to episodic sources like visitor traffic on unpaved roads. In contrast, other peri-urban sites, such as São Pedro, show equal or higher weekday concentrations, likely reflecting work-related freight and mobility. Weekend-weekday differences become negligible across most stations during the rainy season. Table S3 results indicate that pollution exposure is driven more by seasonal factors than by day-of-week variations.

Fig. 5(a)–(d) shows monthly boxplots of daily $PM_{2.5}$, PM_{10}, 2-m temperature, and relative humidity for urban (pink) and peri-urban (blue) sites in 2023. Across January–June (rainy season), urban and peri-urban distributions are similar monthly medians and IQRs for $PM_{2.5}$ and PM_{10} largely overlap, mirroring similar temperature and relative-humidity distributions. From July–November (dry season), urban sites shift higher, especially October–November. Urban boxplots sit above peri-urban for both $PM_{2.5}$ and PM_{10} and show heavier upper tails, indicating more frequent high-concentration days. Meteorological differences between classes remain small relative to the seasonal swing (temperatures rise and RH falls in both groups), so the air-quality gap is concentrated in the dry season, consistent with greater urban exposure to upwind fire corridors. In short, seasonality dominates, but urban concentrations tend to be earlier and higher in the dry season, whereas peri-urban levels track the same pattern at lower central values and with narrower spread.

Fig. S1 shows pairwise Pearson (Pe) and Spearman (Sp) correlations (with p-values) among daily $PM_{2.5}$, PM_{10}, 2-m temperature, and relative humidity, computed separately by season **(a–b)** and area class **(c–d)**. Fig. S1 shows $PM_{2.5}$ and PM_{10} are highly correlated (Pe ≈ 0.94–0.98; Sp ≈ 0.83–0.93; $p < 0.001$), indicating near-proportional co-variation. Temperature and RH is correlated negatively (Pe ≈ −0.66 to −0.75), reflecting the expected thermodynamic anticorrelation. PM versus temperature correlation is low in the rainy season (Pe ≈ 0.03–0.10) but moderate positive in the dry season (Pe ≈ 0.31–0.50), while PM versus RH is correspondingly moderate negative in the dry season (Pe ≈ −0.27 to −0.43) and weak in the rainy season. Urban and peri-urban panels show the same correlation pattern, with only small differences in magnitude. Given the very high correlation between $PM_{2.5}$ and PM_{10}, the associated variance inflation factors (VIFs) would exceed common thresholds (≈5–10), so including both as predictors would introduce severe multicollinearity and unstable coefficient estimates. Treating them as redundant—and prioritizing the greater health relevance of the fine fraction—we used $PM_{2.5}$ as the sole particulate metric (proxy) in the statistical models.

3.2. *Influence of fire and atmospheric conditions on $PM_{2.5}$ concentrations*

To attribute daily $PM_{2.5}$ variability to fire activity and weather—building on the seasonal patterns and WHO exceedances shown above—we fitted Generalized Estimating Equations (GEE) with a Gamma family and log link, treating monitoring sites as clusters and days as the within-cluster time index. $PM_{2.5}$ (the sole particulate outcome, given its strong covariance with PM_{10}; median $PM_{2.5}/PM_{10}$ ≈ 0.79) was aligned by site–day with satellite-derived fire radiative power (FRP) and meteorology. FRP exposure around each site was represented in multiple, physics-aware ways: concentric buffer sums at 25/50/75/100 km, a proximity-weighted composite (heavier weight to nearer fires), and exponential distance-decay indices with decay scales of 30/50/70 km; 1–2-day lags of the composite/decay metrics captured short-term carryover. Temperature and relative humidity were taken exclusively from the in-situ monitoring network. Temperature entered the model only as a natural cubic spline (nonlinear basis; no orthogonalized

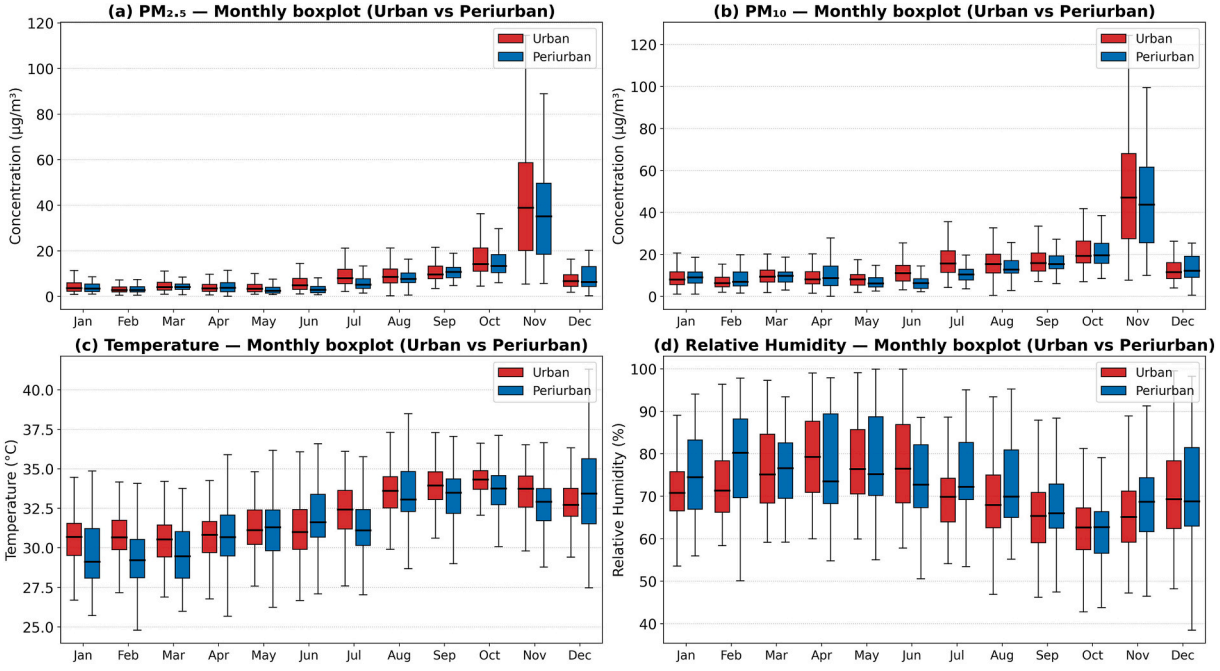

Fig. 5. Monthly distributions (urban vs. peri-urban) monthly boxplots of: (a) daily $PM_{2.5}$, (b) PM_{10}, (c) 2-m air temperature, and (d) Relative humidity for urban (pink) and peri-urban (blue) sites in 2023. Boxes indicate the interquartile range (IQR) with the central line as the median; whiskers summarize the month-to-month spread.

quadratic term was used), while relative humidity entered linearly; we also included an FRP × RH interaction to test humidity-modulated fire effects. ERA5 daily 10-m wind speed, boundary-layer height, and total precipitation (with a 1-day lag) were used as additional controls variables.

All continuous covariates were winsorized (1st–99th percentiles) and standardized (z-scores) prior to modeling; correlation matrices and VIFs were examined to assess collinearity. Temporal dependence within sites was addressed by comparing AR(1) and exchangeable working-correlation structures (with automatic fallback to exchangeable if convergence issues arose). We report coefficients as multiplicative effects $exp(\beta)$ —interpretable as percent change in mean $PM_{2.5}$ per one-SD change in the predictor—and used QIC to compare FRP specifications, decay scales, and correlation structures. Because exploratory diagnostics indicated strong seasonal non-stationarity in fire influence and meteorology, models were estimated separately for January–June (wet season) and July–December (dry season), and results were summarized side-by-side to quantify seasonal shifts in FRP and meteorological sensitivities.

Building on these models, Fig. 6(a) and (b) summarizes how fire activity relates to daily $PM_{2.5}$ and whether that relationship depends on humidity. In the wet season, a +1 SD increase in the standardized FRP index is associated with an ≈10% increase in mean $PM_{2.5}$ ($\exp(\beta)\approx1.10$; $p < 0.001$) under the best-fitting Weighted + Lags • AR1 • d = 70 km specification, lowest QIC (Fig. 6(a)). In the dry season, the corresponding increase is ≈ 25% ($\exp(\beta)\approx1.25$; $p < 0.001$) with Lags_only • Exchangeable • d = 30 km (Fig. 6(a)). Fig. 6(b) shows that the FRP × RH interaction is significant in the wet season: the marginal FRP effect rises from ~4% at RH −1 SD to ~10% at the median and ~16–17% at RH +1 SD ($p \approx 0.047$). In the dry season, the FRP effect remains high but changes little with RH and the interaction is not significant ($p \approx 0.635$). These results indicate that humidity modulates the fire–$PM_{2.5}$ link during the wet months, whereas during the dry months the FRP effect is strong and largely independent of RH over the observed—consistent with a regime where $PM_{2.5}$ levels become dominated by emission magnitude and synoptic-scale advection/mixing rather than local moisture variability.

Fig. 7(a and b) shows the main-effect estimates for the "core" meteorology in the best seasonal GEE models (points = % change in $PM_{2.5}$ per +1 SD; bars = 95% CI; p-values at right). All effects are conditional on FRP and the remaining covariates. In the wet season [Fig. 7(a); Weighted + Lags • AR1 • d = 70], only wind speed is significant and it is positive ($p = 0.026$), indicating that stronger near-surface flow tends to advect smoke into the city when the urban background is otherwise low; PBLH, RH, precipitation (0 and −1 day), and the temperature spline bases are not different from zero ($p \geq 0.05$). In the dry season [Fig. 7(b); Lags-only • EXCH • d = 30], wind speed is negative ($p < 0.001$; ventilation), previous-day precipitation is negative ($p < 0.001$; wet removal), and PBLH is positive ($p < 0.001$; deeper mixed layers coinciding with regional smoke entrainment). Temperature shows weak nonlinearity (one spline term positive, $p = 0.013$); same-day precipitation and the other spline bases are not significant. Meteorological controls on $PM_{2.5}$ are season-dependent: in the wet season, once fire activity is accounted for, most covariates have little residual effect; in the dry season, dispersion (WS), recent rain (Precip-1d), and boundary-layer structure (PBLH) meaningfully modulate concentrations. These results reinforce that fire activity is the primary driver of day-to-day $PM_{2.5}$ variability—particularly during the dry season—while meteorology acts mainly as a conditional modulator of the fire signal.

In accordance with Fig. 7(a–b), Fig. S2 (a)–(b) synthesizes how meteorology influences daily $PM_{2.5}$ across the full set of FRP exposure specifications. In the wet season, Fig. S2 (a), effects cluster near zero and are rarely significant—consistent with low fire activity—except for an occasional small positive wind-speed effect, suggesting episodic smoke advection. In the dry season, Fig. S2 (a), patterns are strong and stable across buffers, decay scales, weighting, and correlation structures: wind speed is consistently negative (ventilation/advection lowers $PM_{2.5}$), PBLH is consistently positive (deeper mixing layers are associated with entrainment/regional smoke, net increasing $PM_{2.5}$), and previous-day precipitation is negative (wet scavenging carryover). Relative humidity and the temperature spline bases remain generally weak once FRP is controlled, reinforcing that dispersion, boundary-layer depth, and wet removal are the dominant meteorological modulators of smoke-driven $PM_{2.5}$ in the dry season.

3.3. *FRP–wind–$PM_{2.5}$ polar radar for operational smoke risk and early warning*

To translate the GEE findings into an operational, city-centered view, we built a four-panel FRP–Wind–$PM_{2.5}$ polar radar that can be

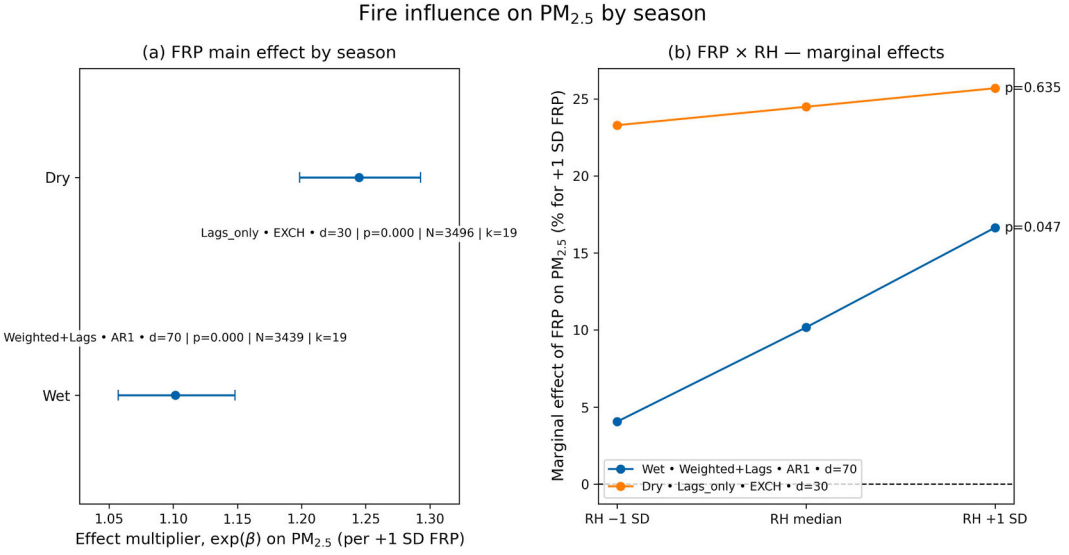

Fig. 6. Fire influence on $PM_{2.5}$ by season: **(a)** Seasonal FRP main effects shown as effect multipliers exp(β) with 95% CIs and p-values; labels indicate the winning specification and data scope (Wet—Weighted + Lags • AR1 • d = 70 km; Dry—Lags_only • EXCH • d = 30 km). Values are percent changes in mean $PM_{2.5}$ per +1 SD in FRP. **(b)** FRP × RH marginal effects from the best model in each season, evaluated at RH = −1 SD, median, and +1 SD; the interaction p-value is annotated at RH = +1 SD.

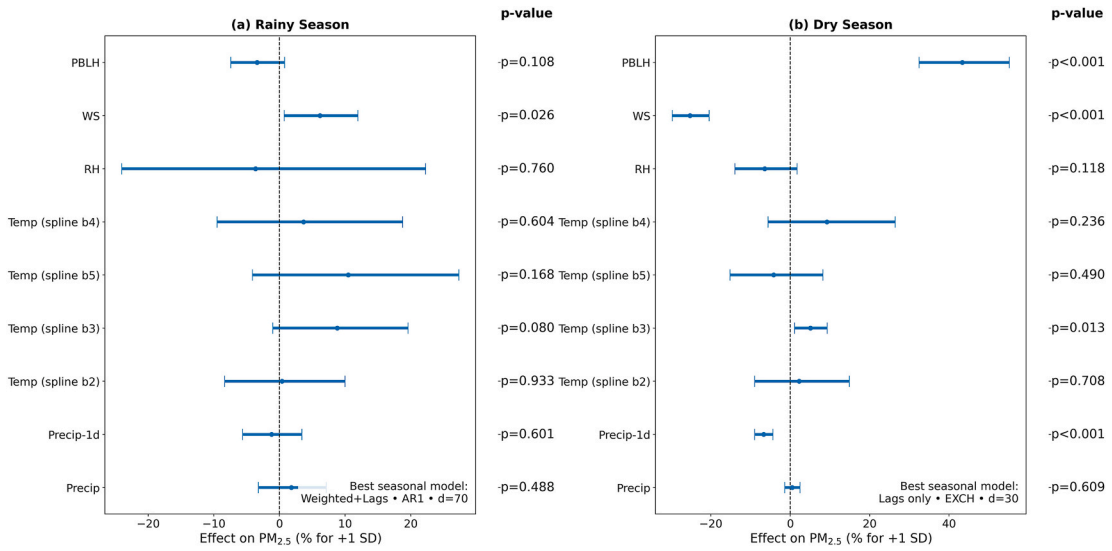

Fig. 7. Core meteorological covariates for the winning seasonal GEE models. Panels show percent change in daily $PM_{2.5}$ per +1 SD in each covariate (points, 95% CIs). **(a)** Rainy season—best model: Weighted + Lags • AR1 • d = 70. **(b)** Dry season—best model: Lags_only • EXCH • d = 30. p-values (≤0.001 precision) are listed at right. Temperature enters as a natural-spline smooth; individual basis coefficients are not directly directional but indicate nonlinearity when significant.

generated at daily to seasonal scales. Each radar is centered on Santarém and uses the same physically motivated exposure settings as the best GEE specifications (upwind cone defined by the daily mean ERA5 wind, ±45°; FRP integrated with distance decay and short lags of 0–1 days with exponential time decay). In all radar panels, the upper-left map shows all MODIS hotspots within 250 km colored by concurrent station $PM_{2.5}$; the upper-right isolates upwind (±45°) sources relative to the station; the lower-left panel is a lag-aware fire-impact index that combines same-day (D0) and previous-day (D–1) upwind FRP with distance decay; and the lower-right panel is a meteorological susceptibility wedge (0–1) determined solely by that day's wind direction and speed at the station. Radial distance is in kilometers, the dashed line marks the mean wind direction (arrow length ∝ wind speed), and captions report total fires and upwind-only counts. These radars provide situational awareness consistent with the modeled effects: they highlight when abundant upwind FRP coincides with favorable advection, the combination most associated with same-day $PM_{2.5}$ elevations in our GEE results.

3.3.1. Case study: November 2023 smoke episode—radar-based situational awareness

On 13 November of 2023, Fig. 8(a)–(d)), upwind activity became established—63 upwind hotspots of 222 total—under easterlies ≈3.7 m/s. The susceptibility wedge centers near ~80°, and the lag-aware impact field lights up tiles within ~100–150 km, indicating moderate potential from D0 + D–1 exposure. Conditions intensify on 14 Nov [Fig. 8(e)–(h)]: total fire load and, crucially, upwind sources increase sharply (169 upwind of 1550 total) while easterlies ≈3.4 m/s persist. The impact field expands to ~200–250 km as the D–1 carry-over from 13 Nov stacks with same-day emissions, and the station $PM_{2.5}$ markers simultaneously darken—consistent with the observed deterioration in air quality.

A longer chronology in the Supplement supports this interpretation. Fig. S3 (10-11 November) and Fig. S4 (12 November) shows the pre-peak phase with few upwind ignitions (6/27 and 13/80, respectively) and only localized impact tiles despite suitable easterlies, consistent with low immediate risk. After the 13–14 November surge, Fig. S5 (15 November) documents a drop in same-day upwind fires (6/144), yet the lag-aware impact index remains elevated and aligned with ~4.7 m/s easterlies—evidence that D–1 transport from 14 November can sustain smoke even as new ignitions wane. Fig. S6 (16 November) shows a rebound in upwind activity (98/682) under ~3.4 m/s easterlies and a renewed, spatially extensive impact field, indicating continued transport potential.

A second episode of fire-driven $PM_{2.5}$ deterioration, followed by rapid recovery, occurred immediately after the prior peak (18–21 November). Fig. 9 synthesizes 19–20 November, with the flanking days shown in Fig. S7 (18 November) and Fig. S8 (21 November). On 18 November (Fig. S7), many ignitions appeared within 250 km of the city (243 total; 80 upwind within ±45° of the mean wind), and the lag-aware upwind impact index showed several red/yellow sectors along the NE corridor under easterly–northeasterly 3–4 m/s flow and high meteorological susceptibility—conditions consistent with the onset of a smoke build-up. Activity intensified on 19 November [Fig. 9(a)–(d)]: 491 total fires (but only 64 upwind-aligned), yet the susceptibility lobe remained strong toward the NE; the upwind index still flagged multiple high-risk sectors, and the central monitor showed elevated $PM_{2.5}$. The situation improved sharply on 20 November [Fig. 9(e)–(h)] as regional fire activity collapsed (30 total; 22 upwind) and the upwind index weakened, even though winds and the susceptibility pattern changed little; measured $PM_{2.5}$ concurrently declined, indicating that the drop in the source term dominated day-to-day air-quality changes. A rebound on 21 Nov (Fig. S8) is evident—403 total fires; 157 upwind—with renewed high values in the lag-aware upwind index under similar NE flow and a persistent susceptibility lobe.

Fig. 10 shows the daily mean urban–periurban $PM_{2.5}$ (blue) with the weighted number of upwind fire hotspots (red) from July–December 2023, dry season, with the 10–22 November episode shaded. Over the full period the two series co-vary with a moderate but significant association (Pearson $r = 0.522$; Spearman $\rho = 0.655$; both $p < 0.001$). During the mid-November event—when the polar radar indicated a dense corridor of upwind fires together with high meteorological susceptibility toward the city (Fig. 8; Fig. 9; and Fig. S3–S8)— the source–receptor coupling strengthened markedly (Pearson $r = 0.758$, $p = 0.003$; Spearman $\rho = 0.857$, $p < 0.001$). The higher rank correlation than linear correlation indicates a monotonic but slightly nonlinear response, consistent with the log-link GEE results and with occasional saturation at very high smoke loads.

Event timing in Fig. 10 also mirrors the radar-diagnosed transport: the $PM_{2.5}$ peaks on 13–14 and 19 November coincide with (or follow by 0–1 day) surges in upwind fire activity detected by the radar, while the rapid improvement after 20 November aligns with both a sharp drop in upwind fires and a shift to less favorable advection (lower susceptibility

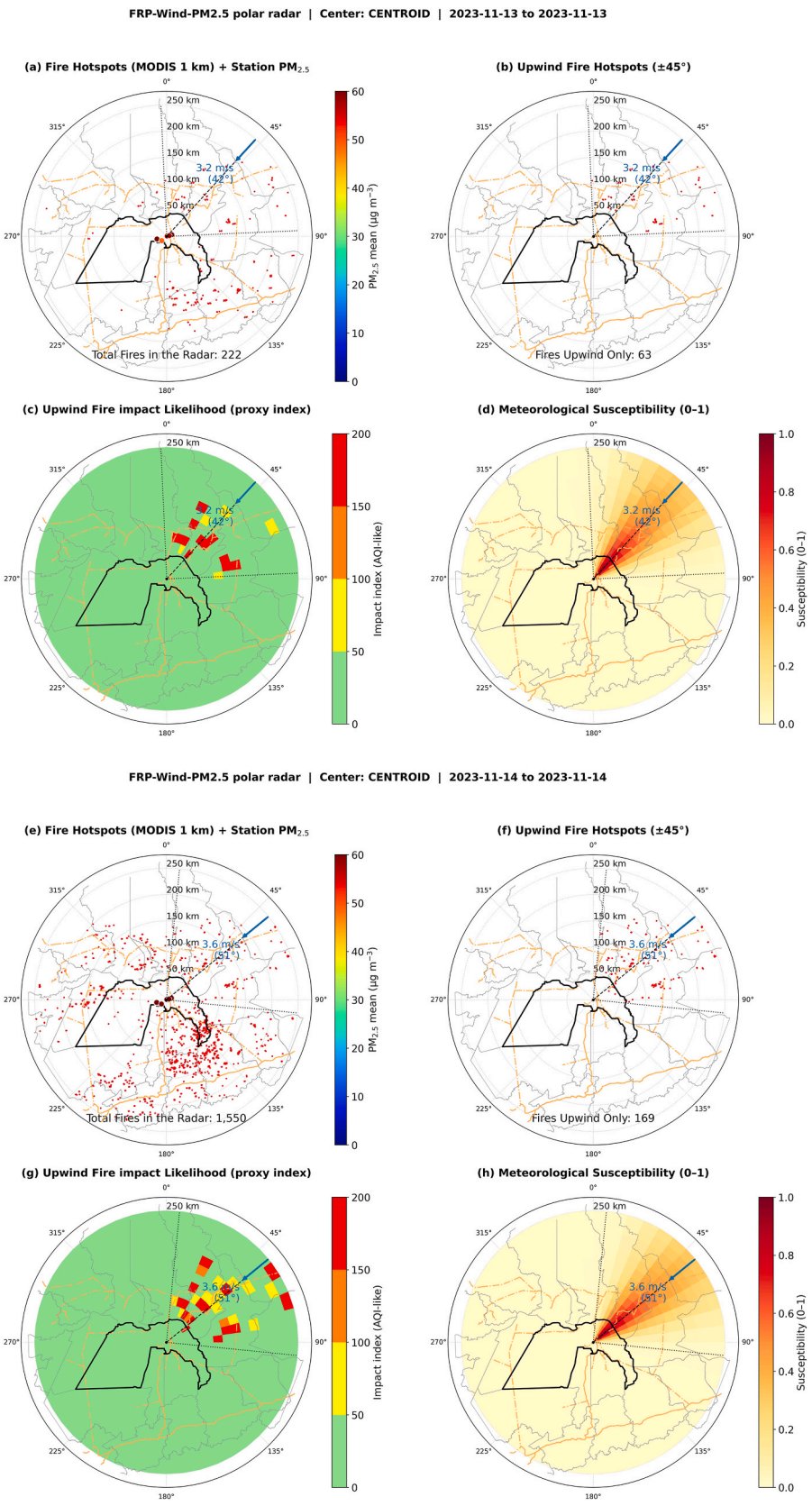

Fig. 8. Lag-aware FRP–Wind–$PM_{2.5}$ polar radar for 13–14 November 2023. Panels **(a)–(d)**: 13 November; **(e)–(h)**: 14 November. For each day—**(a)–(e)**: all MODIS hotspots ≤250 km with station $PM_{2.5}$; **(b)–(f)**t: upwind hotspots (±45° about mean wind); **(c)–(g)**: lag-aware (D0 + D−1, distance-weighted) upwind fire-impact index; **(d)–(h)**: wind-based susceptibility (0–1). Concentric rings mark 50–250 km; labels report total/upwind fires.

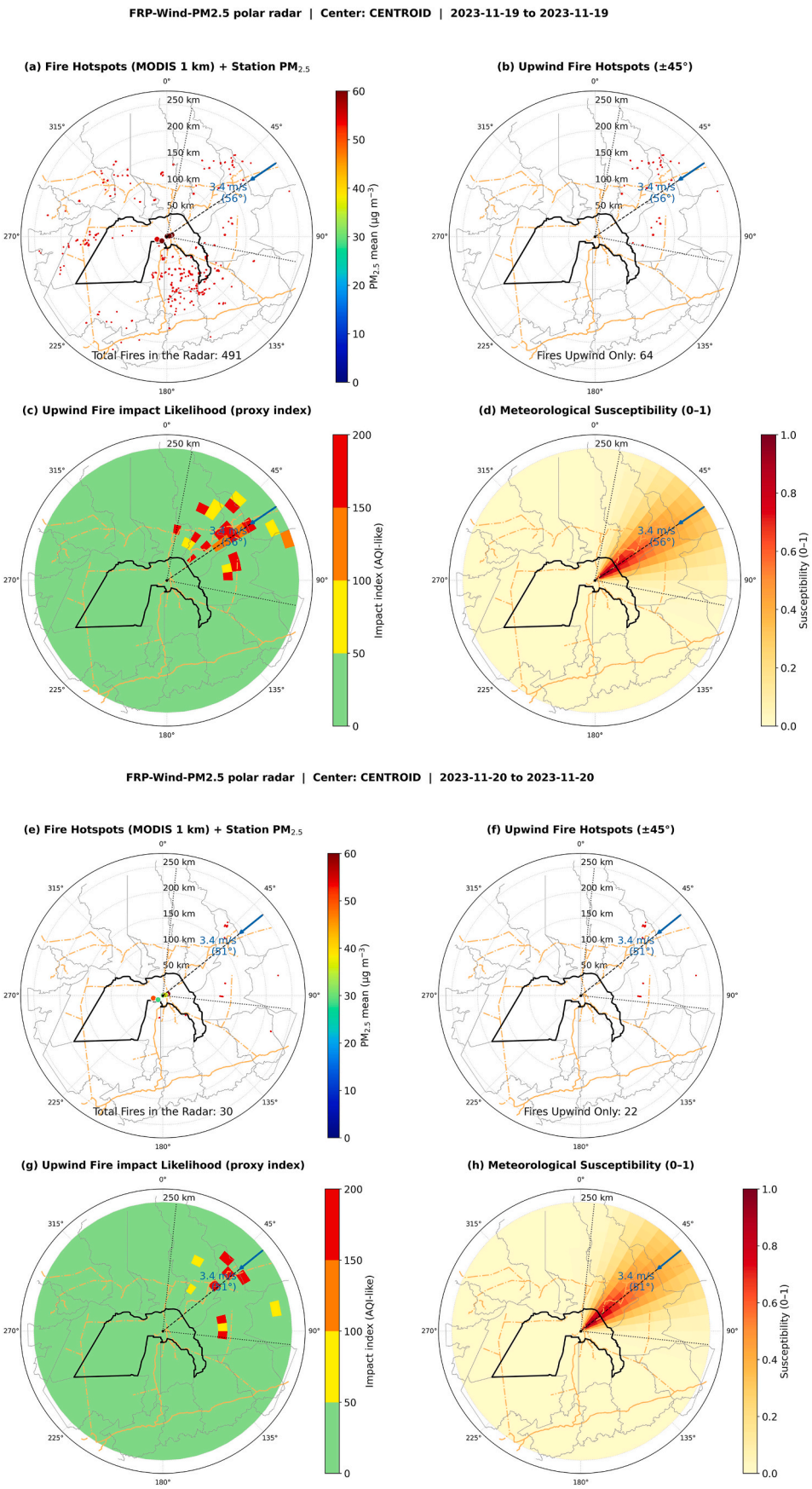

Fig. 9. Lag-aware FRP–Wind–$PM_{2.5}$ polar radar for 19–20 November 2023. Panels **(a)–(d)**: 19 November; **(e)–(h)**: 20 November. For each day**—(a)–(e):** all MODIS hotspots ≤250 km with station $PM_{2.5}$; **(b)–(f)**t: upwind hotspots (±45° about mean wind); **(c)–(g):** lag-aware (D0 + D−1, distance-weighted) upwind fire-impact index; **(d)–(h):** wind-based susceptibility (0–1). Concentric rings mark 50–250 km; labels report total/upwind fires.

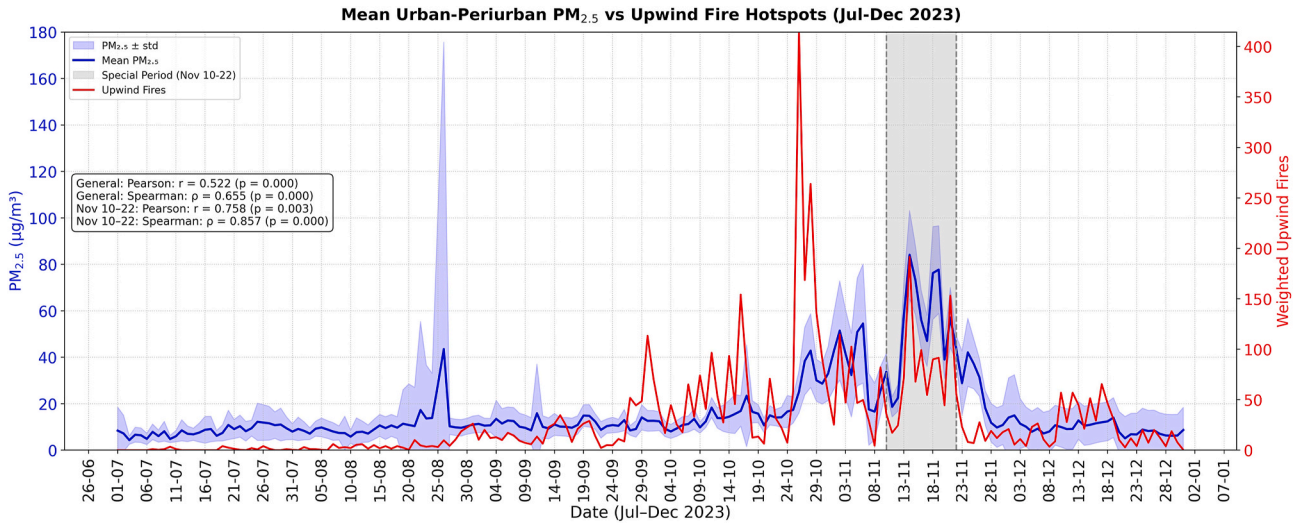

Fig. 10. Daily mean $PM_{2.5}$ concentrations and upwind fire hotspots in Santarém, Brazil (July-December 2023). The blue line shows average $PM_{2.5}$ levels across urban and periurban stations (±1 standard deviation), while the red line represents weighted upwind fire counts calculated with 0-1 day lags within a 250 km radius and 45° upwind sector. The gray shaded area indicates the period of elevated pollution and fire activity (10-22 November 2023). Correlation statistics for both the entire period and the highlighted period are shown.

in the radar panels). Taken together, the analysis identifies three necessary conditions for an acute urban smoke intrusion episode: (i) active fires in the upwind sector, (ii) advection-favorable wind fields, and (iii) short-lag persistence of emissions (D0 + D–1). The strongest $PM_{2.5}$ degradation (14 November) occurred with all three conditions met, whereas elevated risk persisted on 15 November due to favorable winds and prior-day loading despite fewer new fires. This lag-sensitive behavior corroborates the GEE findings and further validates the polar radar as a physically grounded tool for near-term smoke risk assessment.

4. Discussion

The pronounced seasonal pattern observed in Santarém—characterized by low and stable particulate matter concentrations during the rainy season and sharply elevated levels with significant spatial heterogeneity during the dry season—is a hallmark of the Amazonian biomass burning regime. This aligns with some regional research documenting the transboundary nature of fire emissions and their role as the dominant source of fine particulates during the dry season (Artaxo et al., 2013; Reddington et al., 2015). The consistently high $PM_{2.5}/PM_{10}$ ratios (0.7–0.9) from September to November provide direct, ground-based confirmation of a shift to fine-mode aerosol dominance, a known chemical fingerprint of biomass burning smoke that has been previously identified in atmospheric sampling studies (Martin et al., 2010).

The earlier and more intense pollution spikes recorded at peri-urban stations reviews an important local dynamic often missed by regional models. This suggests that these areas, which interface directly with fire-prone landscapes, may experience a more immediate and potent impact from local burning activities—such as agricultural clearing and forest fires—compared to the urban core, which is likely influenced by a more diluted regional smoke plume alongside its distinct urban emission sources (Cardoso et al., 2020). Consequently, while our findings affirm the established macro-scale narrative of long-range smoke transport, they also reveal a finer-scale, intra-city heterogeneity in exposure, showing that populations in the urban periphery may face a disproportionately high health risk during the burning season.

The synchronicity of positive temperature anomalies, negative humidity anomalies, and elevated particulate matter concentrations during the dry season, as revealed by the standardized anomalies, reveals the coupled nature of fire weather and pollution accumulation. This triad of conditions (simultaneous occurrences of temperature, humidity particulate matter concentrations anomalies) is not merely coincidental but physically interdependent: the same persistent high-pressure systems and reduced cloud cover that foster elevated temperatures and lower relative humidity also inhibit pollutant dispersion through a suppressed boundary layer, while concurrently creating the dry fuel conditions ideal for ignition and fire spread. This aligns with the regional pattern described by Reddington et al. (2015), where drought conditions intensify burning and suppress atmospheric mixing, leading to the accumulation of pollutants. The fact that this meteorological signature is so clearly captured by the sensor network validates its utility in diagnosing the fundamental drivers of air quality extremes. Furthermore, the tight coupling observed suggests a potential positive feedback loop, where regional smoke from fires may further intensify the dry, warm conditions that favor their ignition and persistence. This finding moves beyond establishing a seasonal correlation and begins to delineate the specific atmospheric states that culminate in the highest exposure events for the urban population, thereby pinpointing important windows for public health intervention.

The spatiotemporal analysis further reveals that while urban and peri-urban areas share a common seasonal pattern, their exposure profiles differ in some ways. The earlier and more intense pollution anomalies in peri-urban zones point to their role as sentinels for initial smoke intrusion, likely due to their proximity to active fire frontiers. The subsequent, even higher-amplitude peaks in the urban core later in the dry season suggest the accumulation of regional smoke plume, potentially compounded by local urban emissions. This spatial gradient in the timing and intensity of exposure reveals that populations across the city face heterogeneous health risks throughout the fire season. Importantly, the overwhelming concentration of WHO guideline exceedances (>94%) within the dry season, coupled with the systematic shift to a fine-particle-dominated aerosol ($PM_{2.5}/PM_{10}$ ratio ~0.79), demonstrates that the public health burden is not only seasonal but also driven by the most respirable and hazardous particle fraction. The minimal weekend-weekday effect, dwarfed by this seasonal signal, reinforces that the primary driver of population exposure is large-scale biomass burning, not local weekly activity cycles.

The divergence in particulate matter distributions between urban and peri-urban areas during the peak of the dry season, as detailed in Fig. 5, refines the understanding of intra-city exposure dynamics. While both zones are subject to the same regional smoke plume, the

consistently higher medians and heavier upper tails in urban boxplots from October to November indicate that the urban core experiences a more concentrated and persistent pollution burden during the most polluted period. This urban amplification effect cannot be explained towards the combined impact of advected biomass burning smoke and localized urban emissions.

The GEE models quantitatively confirm that fire activity is a dominant driver of $PM_{2.5}$ variability in Santarém, with a effect size that intensifies significantly from the wet to the dry season. The fivefold increase in the FRP coefficient (from ~10% to ~25% increase in $PM_{2.5}$ per +1 SD FRP) quantitatively captures the transition from a regime where fires are sporadic and weakly influential to one where they are the principal determinant of air quality. The significant FRP × RH interaction during the wet season suggests that in a generally clean atmosphere, the hygroscopic growth and aerosol chemistry modulated by humidity can enhance the impact of isolated fire plumes. In contrast, the absence of this interaction in the dry season indicates a saturation effect, where the massive, regional-scale smoke burden overwhelms local meteorological modulation; the $PM_{2.5}$ levels are then primarily a function of emission strength and synoptic-scale transport, as noted in large-scale analyses of Amazonian aerosol (Artaxo et al., 2013). This important, seasonally-stratified quantification of the fire-$PM_{2.5}$ relationship provides the empirical foundation necessary to build predictive systems and underscores that fire management is the single most effective lever for protecting public health during the critical dry months.

Furthermore, GEE models further clarified the distinct seasonal roles of meteorology in modulating $PM_{2.5}$ concentrations, once fire activity is accounted for. The shift in wind speed's effect—from a weakly positive influence in the wet season, likely advecting distant smoke, to a significant ventilating effect in the dry season—highlights a fundamental change in atmospheric processes. The consistent negative coefficient for previous-day precipitation during the dry season robustly confirms the importance of wet scavenging as a key cleansing mechanism. Perhaps most notably, the positive association between boundary layer height (PBLH) and $PM_{2.5}$ in the dry season reveals a critical dynamic: deeper mixing layers do not necessarily dilute local pollution but are instead correlated with the large-scale entrainment of regionally aged smoke, a phenomenon documented in Amazonian atmospheric studies (Andreae et al., 2015). The stability of these meteorological effects across the suite of FRP exposure specifications (Fig. S2) underscores their robustness. Ultimately, these findings demonstrate that while meteorology acts as a secondary modulator, its influence is conditional on the primary source term; its most meaningful impacts on $PM_{2.5}$ are only realized when and where significant fire emissions are present.

The November 2023 case study demonstrates the operational utility of the FRP–Wind–$PM_{2.5}$ polar radar as a tool for situational awareness. It visually encapsulates the dynamic process of smoke transport, moving beyond static correlation to reveal how air quality deteriorates in near-real-time through the interplay of three factors: the intensification of upwind fire clusters, persistent wind direction aligning these sources with the receptor area, and the cumulative effect of multi-day emissions. The tool's critical advancement is its ability to integrate this spatial alignment with a temporal lag, as evidenced on 15 November when elevated $PM_{2.5}$ levels persisted due to the transport of the previous day's emissions, despite a drop in new ignitions. This lag-aware impact field provides a more accurate and physically plausible assessment of risk than a simple snapshot of daily fire counts. Consequently, this methodology translates the statistical relationships quantified by the GEE models into a practical, low-computational framework for identifying emerging smoke corridors and forecasting short-term degradation in air quality, fulfilling a key objective of providing actionable intelligence for public health protection in data-scarce regions.

The second episode, 18–20 November, reinforces an important finding for public health preparedness: during the peak of the fire season, day-to-day changes in air quality are predominantly driven by the highly variable ignition field not only by the synoptic-scale meteorology. The rapid deterioration and subsequent recovery observed between 19 and 20 November occurred despite largely consistent wind patterns and atmospheric susceptibility. This demonstrates that while meteorological corridors create the potential for transport, the actualization of high-$PM_{2.5}$ events is contingent on the presence of active upwind fires. The system's sensitivity to this ignition dynamic is a key operational insight; it suggests that monitoring the location and intensity of fire activity within established wind corridors can provide reliable short-term forecasts of impending air quality degradation, even in the absence of major meteorological shifts. This further validates the core premise of the early-warning tool, highlighting its utility in tracking the highly transient source term that ultimately governs exposure risk during the crisis period of the burning season.

The strong, event-driven correlation between upwind fire hotspots and urban $PM_{2.5}$, as quantified in Fig. 10, provides an important statistical validation of the physical relationships visualized by the polar radar. The significant strengthening of this correlation during the mid-November episode confirms that the tool successfully identifies periods when the source-receptor connection is most direct and potent. The higher Spearman's rho indicates a robust, monotonic relationship that accommodates the non-linear saturation effects typical of extreme pollution events, a nuance that aligns with the Gamma model's structure. Ultimately, this integrated analysis consolidates the three necessary and sufficient conditions for a significant urban smoke intrusion: the presence of upwind fires, wind fields capable of advecting emissions toward the city, and the cumulative contribution of multi-day burning. The fact that the most severe $PM_{2.5}$ peaks materialize only when these conditions converge emphasize that effective early warning must move beyond tracking fires or wind in isolation. Instead, it must fuse these elements into a unified, lag-aware assessment, as demonstrated here, to accurately anticipate the acute exposure events that pose the greatest threat to public health.

In conclusion, this study provides a city-scale, physics-informed assessment that quantitatively links biomass burning to the air quality crisis in Santarém, a representative medium-sized city in the Amazon. By integrating a network of low-cost sensors with satellite fire data and reanalysis meteorology, we have moved beyond broad seasonal correlations to deliver a mechanistic understanding of the drivers of $PM_{2.5}$. These results systematically establish that the extreme degradation of air quality is a direct consequence of upwind fire activity, the intensity of which is modulated by specific meteorological conditions—particularly wind direction and boundary layer processes. The statistical models quantified the seasonally varying effect sizes of fire, while the novel polar radar tool translated these relationships into an operational framework for situational awareness.

Despite the strengths of this integrated framework, limitations must be acknowledged when interpreting the results. First, the MODIS-based FRP product offers only one daytime overpass per sensor, which increases uncertainty in the detection of short-lived or low-intensity fires; these smaller ignitions may extinguish before the satellite pass and thus remain unobserved, leading to an underestimation of the true ignition field. Second, although the low-cost sensors employed here have been validated, they remain subject to operational challenges—including humidity sensitivity, electronic drift, and the need for regular maintenance—similar to those affecting reference-grade instruments. Third, long-range smoke transport from distant regions of the Amazon basin can influence air quality in Santarém during enhanced burning episodes; such remote contributions cannot be fully disentangled using local FRP metrics alone. Fourth, the complex lake–river breeze dynamics characteristic of the Tapajós–Amazon confluence may impact pollutant dispersion in ways that are not fully captured by the reanalysis wind fields used in this study, particularly at sub-grid scales. Finally, because the monitoring network does not measure wind speed or wind direction, we relied on ERA5 reanalysis for these variables; although ERA5 performs well at regional scales, its ~31 km resolution cannot resolve fine-scale circulations, introducing additional uncertainty into the modeled

transport pathways. These limitations do not compromise the central findings but highlight key areas where future work, including multi-year analyses, higher-frequency fire products, local wind measurements, and plume-rise modeling—could further refine exposure assessments in Amazonian cities.

While this study utilized ERA5 reanalysis data for analysis, the developed tool is designed for operational forecasting and can be seamlessly adapted to utilize real-time meteorological prediction data, such as the Global Forecast System (GFS), and generate forecasts on an hourly basis. This integrated data-modeling approach demonstrates that it is not merely the presence of fires, but their precise location relative to wind corridors and their cumulative impact over days, that determines urban exposure. By providing a scalable and transferable methodology, this work addresses a critical gap in environmental monitoring for developing Amazonian cities, offering a scientifically-grounded, actionable pathway for protecting public health where formal infrastructure is limited. It emphasizes that effective air quality management on the Amazon must prioritize targeted fire prevention and preparedness, informed by local-scale, real-time monitoring and forecasting.

5. Conclusions

This work establishes a direct, quantitative link at the city-scale between biomass burning and the severe particulate matter pollution plaguing Santarém, a key Amazonian urban center. This integrated methodology, fusing a network of low-cost sensors with satellite fire data and reanalysis meteorology, yielded several important findings. This study systematically confirmed that the extreme dry-season degradation of air quality is a direct consequence of upwind fire activity, with the effect of Fire Radiative Power (FRP) on $PM_{2.5}$ increasing fivefold from the wet (≈10% increase per +1 SD FRP) to the dry season (≈25% increase). This relationship is modulated by a triad of meteorological conditions—elevated temperature, lower humidity, and specific boundary-layer processes—that concurrently favor fire spread and pollution accumulation. The results for the year 2023 revealed significant intra-city heterogeneity in exposure. Peri-urban areas act as sentinels, experiencing earlier and more intense initial smoke intrusion, while the urban core later suffers from a more concentrated and persistent pollution burden, likely due to the combined impact of regional smoke plumes and local urban emissions. This spatial gradient, coupled with the finding that over 94% of WHO guideline exceedances occur during the dry season and are dominated by fine particles ($PM_{2.5}$/PM_{10} ratio ~0.79), underscores a spatially and temporally variable public health risk. The statistical models and the novel FRP–Wind–$PM_{2.5}$ polar radar tool developed here translate this information into actionable intelligence. The tool demonstrates that the actualization of high-risk episodes depends on three convergent factors: (i) active upwind fires, (ii) wind corridors aligned with the urban area, and (iii) the cumulative impact of multi-day emissions. By providing a lag-aware, physically plausible assessment of transport risk, this low-computational approach offers a scalable and transferable solution for near-real-time situational awareness and early warning in data-scarce regions across the Amazon. Ultimately, this work emphasizes that effective air quality management in the communities and developing cities in Amazon must prioritize targeted fire prevention and preparedness. The findings provide a scientific foundation for public health interventions that are informed by local-scale, real-time monitoring and forecasting, offering a tangible pathway to mitigate exposure for vulnerable urban populations.

CRediT authorship contribution statement

Domingas de Oliveira Almeida: Writing – review & editing, Writing – original draft, Visualization, Validation, Supervision, Software, Resources, Methodology, Investigation, Funding acquisition, Formal analysis, Data curation, Conceptualization. **Ana Carla dos Santos Gomes:** Writing – review & editing, Writing – original draft, Validation, Supervision, Software, Resources, Project administration, Methodology, Investigation, Funding acquisition, Formal analysis, Data curation, Conceptualization. **Sarah Suely Alves Batalha:** Supervision, Data curation. **Tiago Bentes Mandú:** Supervision, Data curation. **Fernanda Souza do Nascimento:** Writing – review & editing, Supervision. **Glauce Vitor da Silva:** Writing – review & editing, Supervision, Data curation. **Maria João Costa:** Supervision. **Ediclê de Souza Fernandes Duarte:** Writing – review & editing, Writing – original draft, Visualization, Validation, Supervision, Software, Methodology, Investigation, Formal analysis, Data curation, Conceptualization.

Ethical approval

Not applicable.

Funding

This study was funded by the Amazon Foundation for Studies and Research Support (FAPESPA).

Declaration of competing interest

The authors declare no competing interests.

Acknowledgements

The authors would like to thank the Amazon Foundation for Supporting Studies and Research (FAPESPA) for the funding, and everyone involved in the project "*Pilot Network for Innovation in Air Quality Monitoring in the Western Pará Region: Guardians of the Air*" for collecting data. This study was financed in part by the *Coordenação de Aperfeiçoamento de Pessoal de Nível Superior - Brazil* (CAPES) - Finance Code 001, Brazil, for the master scholarship granted.

Appendix A. Supplementary data

Supplementary data to this article can be found online at https://doi.org/10.1016/j.jenvman.2026.128875.

Data availability

Data will be made available on request.

References

Al Ahasan, M.A., Roy, S., Saim, A.H.M., Akter, R., Hossain, M.Z., 2018. Arduino-based real time air quality and pollution monitoring system. Int. J. Innov. Res. Comput. Sci. Technol. 6 (4). https://doi.org/10.2139/ssrn.3531764.

Alahmad, B., Khraishah, H., Althalji, K., Borchert, W., Al-Mulla, F., Koutrakis, P., 2023. Connections between air pollution, climate change, and cardiovascular health. Can. J. Cardiol. 39 (9), 1182–1190. https://doi.org/10.1016/j.cjca.2023.03.025.

Almeida, D.O., Santos Gomes, A.C., Alves Batalha, S.S., Vitor da Silva, G., Bentes Mandú, T., Tapajos Silva, R.P., Silva Dias, G., 2025. Variabilidade na Qualidade do Ar: uma Abordagem Comparativa entre Zonas Urbana e Periurbana em Santarém, Pará. Rev. Bras. Geogr. Fis. 18 (2), 863–879. https://doi.org/10.26848/rbgf.v18.2.p863-879.

Almeida, D.O., Gomes, A.C.S., Batalha, S.S.A., Silva, G.V., Cordeiro Junior, L.G., Martins, E.A.I., Raiol, A.S., 2023. Monitoring atmospheric pollution in Central Amazon: case study carried out in Santarém City – PA. J. Hyperspectral Remote Sens. 13 (2), 187–201. https://doi.org/10.29150/jhrs.v13.2.p187-201.

Alonso-Pérez, S., López-Solano, J., 2023. Long-term analysis of aerosol concentrations using a low-cost sensor: monitoring African dust outbreaks in a suburban environment in the Canary Islands. Sensors 23, 7768. https://doi.org/10.3390/s23187768.

Alves, N.O., Vessoni, A.T., Quinet, A., Fortunato, R.S., Kajitani, G.S., Peixoto, M.S., 2017. Biomass burning in the Amazon region causes DNA damage and cell death in human lung cells. Sci. Rep. 7, 10937. https://doi.org/10.1038/s41598-017-11024-3.

Ananth, C.V., Preisser, J.S., 1999. Bivariate logistic regression: modelling the association of small for gestational age births in twin gestations. Stat. Med. 18 (15), 2011–2023. https://doi.org/10.1002/(SICI)1097-0258(19990815)18:15<2011::AID-SIM169>3.0.CO;2-8.

Andrade, A.C., Galvani, E., Souza, P.H., 2024. Performance of an alternative system for monitoring and collecting meteorological data. ES Eng. Sci. 13 (4). https://doi.org/10.18607/ES20241318419.

Andreae, M.O., Acevedo, O.C., Araùjo, A., Artaxo, P., Barbosa, C.G.G., Barbosa, H.M.J., Brito, J., Carbone, S., Chi, X., Cintra, B.B.L., Da Silva, N.F., Dias, N.L., Dias-Júnior, C. Q., Ditas, F., Ditz, R., Godoi, A.F.L., Godoi, R.H.M., Heimann, M., Hoffmann, T., Yáñez-Serrano, A.M., 2015. The Amazon Tall Tower Observatory (ATTO): overview of pilot measurements on ecosystem ecology, meteorology, trace gases, and aerosols. Atmos. Chem. Phys. 15, 10723–10776. https://doi.org/10.5194/acp-15-10723-2015.

Artaxo, P., Gatti, A.M.C., Leal, K.M., Longo, S.R., Freitas, L.L., Lara, T.M., Pauliquevis, A. S., Rizzo, L.V., Procópio, 2005. Química atmosférica na Amazônia: a floresta e as emissões de queimadas controlando a composição da atmosfera amazônica. Acta Amazonica 35, 185–192. https://doi.org/10.1590/S0044-59672005000200008.

Artaxo, P., Rizzo, L.V., Brito, J.F., Barbosa, H.M.J., Arana, A., Sena, E.T., Cirino, G.G., Bastos, W., Martin, S.T., Andreae, M.O., 2013. Atmospheric aerosols in Amazonia and land use change: from natural biogenic to biomass burning conditions. Faraday Discussions 165, 203. https://doi.org/10.1039/c3fd00052d.

Blaga, R., Gautam, S., 2024. Improving PM10 sensor accuracy in urban areas through calibration in Timişoara. npj Clim. Atmos. Sci. 7, 268. https://doi.org/10.1038/s41612-024-00812-0.

Božilov, A., Tasić, V., Živković, N., Lazović, I., Blagojević, M., Mišić, N., Topalović, D., 2022. Performance assessment of NOVA SDS011 low-cost PM sensor in various microenvironments. Environ. Monit. Assess. 194, 595. https://doi.org/10.1007/s10661-022-10290-7.

Cardoso, A.C.D., Oliveira, K.D., Pinho, T.V.G., 2020. Mismatches between extended urbanization and everyday socioenvironmental conflicts in Santarém, Pará, Brazil. Sustentab. Debate 11 (1), 83–97. https://doi.org/10.18472/SustDeb.v11n1.2020.29468.

Deroubaix, A., Hoelzemann, J.J., Ynoue, R.Y., De Almeida Albuquerque, T.T., Alves, R. C., De Fatima Andrade, M., Andreão, W.L., Bouarar, I., De Souza Fernandes Duarte, E., Elbern, H., Franke, P., Lange, A.C., Lichtig, P., Lugon, L., Martins, L.D., De Arruda Moreira, G., Pedruzzi, R., Rosario, N., Brasseur, G., 2024. Intercomparison of air quality models in a megacity: toward an operational ensemble forecasting system for São Paulo. J. Geophys. Res. Atmos. 129. https://doi.org/10.1029/2022jd038179 e2022JD038179.

de Almeida Albuquerque, T.T., De Fátima Andrade, M., Ynoue, R.Y., Moreira, D.M., Andreão, W.L., Santos, F.S.D., Nascimento, E.G.S., 2018. WRF-SMOKE-CMAQ modeling system for air quality evaluation in São Paulo megacity with a 2008 experimental campaign data. Environ. Sci. Pollut. Res. 25, 36555–36569. https://doi.org/10.1007/s11356-018-3583-9.

de Fatima Andrade, M., Ynoue, R.Y., Freitas, E.D., Todesco, E., Vela, A.V., Ibarra, S., Martins, L.D., Martins, J.A., Carvalho, V.S.B., 2015. Air quality forecasting system for Southeastern Brazil. Front. Environ. Sci. 3, 9. https://doi.org/10.3389/fenvs.2015.00009.

de Souza, P., Nthusi, V., Klopp, J., Shaw, B., Ho, W., Saffell, J., 2017. Ratti A Nairobi experiment in using low cost air quality monitors. Clean Air J. 27 (2), 12–42. https://doi.org/10.17159/2410-972X/2017/v27n2a6.

de Souza Fernandes Duarte, E., Franke, P., Lange, A.C., Friese, E., Da Silva Lopes, F.J., Da Silva, J.J., Reis, J.S.D., Landulfo, E., Silva, C.M.S.E., Elbern, H., Hoelzemann, J.J., 2021. Evaluation of atmospheric aerosols in the metropolitan area of São Paulo simulated by the regional EURAD-IM model on high-resolution. Atmos. Pollut. Res. 12, 451–469. https://doi.org/10.1016/j.apr.2020.12.006.

de Souza Fernandes Duarte, E., Lucio, P.S., Costa, M.J., Salgueiro, V., Salgado, R., Potes, M., Hoelzemann, J.J., Bortoli, D., 2024. Pollutant-meteorological factors and cardio-respiratory mortality in Portugal: seasonal variability and associations. Environ. Res. 240, 117491. https://doi.org/10.1016/j.envres.2023.117491.

de Souza Fernandes Duarte, E., Lucio, P.S., Henriques-Rodrigues, L., Costa, M.J., 2025. Impact of monthly air pollution and weather conditions on cardiorespiratory mortality in Portuguese Metropolitan areas. Sci. Rep. 15, 4147. https://doi.org/10.1038/s41598-025-88473-8.

de Souza Fernandes Duarte, E., Salgueiro, V., Costa, M.J., Lucio, P.S., Potes, M., Bortoli, D., Salgado, R., 2023. Fire-pollutant-atmosphere components and its impact on mortality in Portugal during wildfire seasons. GeoHealth 7. https://doi.org/10.1029/2023GH000802 e2023GH000802.

de Souza Tadano, Y., Potgieter-Vermaak, S., Siqueira, H.V., Hoelzemann, J.J., Duarte, E. S.F., Alves, T.A., Valebona, F., Lenzi, I., Godoi, A.F.L., Barbosa, C., Ribeiro, I.O., De Souza, R.a.F., Yamamoto, C.I., Santos, E., Fernandesi, K.S., Machado, C., Martin, S. T., Godoi, R.H.M., 2024. Predicting health impacts of wildfire smoke in Amazonas basin, Brazil. Chemosphere 367, 143688. https://doi.org/10.1016/j.chemosphere.2024.143688.

de Souza, A., de Medeiros, E.S., de Oliveira-Júnior, J.F., et al., 2025. Analyzing maximum temperature trends and extremes in Brazil: a study of climate variability and anthropogenic influences from 1960 to 2020. Aerosol Sci Eng. https://doi.org/10.1007/s41810-025-00288-2.

Freitas, S.R., Longo, K.M., Dias, M.a.F.S., Dias, P.L.S., Chatfield, R., Prins, E., Artaxo, P., Grell, G.A., Recuero, F.S., 2005. Monitoring the transport of biomass burning emissions in South America. Environ. Fluid Mech. 5, 135–167. https://doi.org/10.1007/s10652-005-0243-7.

Genikomsakis, K.N., Galatoulas, N.-F., Dallas, P.I., Ibarra, L.M.C., Margaritis, D., Ioakimidis, C.S., 2018. Development and On-Field testing of low-cost portable system for monitoring PM2.5 concentrations. Sensors 18, 1056. https://doi.org/10.3390/s18041056.

Giglio, L., Boschetti, L., Roy, D.P., Humber, M.L., Justice, C.O., 2016. The collection 6 MODIS burned area mapping algorithm and product. Remote Sens. Environ. 217, 72–85. https://doi.org/10.1016/j.rse.2018.05.018.

Giglio, L., et al., 2003. An enhanced contextual fire detection algorithm for MODIS. Remote Sens. Environ. 87, 273–282. https://doi.org/10.1016/S0034-4257(03)00184-6.

Hardin, J.W., Hilbe, J.M., 2013. Generalized Estimating Equations. Chapman & Hall/CRC.

Hersbach, H., et al., 2020. The ERA5 global reanalysis. Q. J. R. Meteorol. Soc. 146, 1999–2049. https://doi.org/10.1002/qj.3803.

Hoelzemann, J.J., Longo, K.M., Fonseca, R.M., Rosário, N.M.E., Elbern, H., Freitas, S.R., 2009. Regional representativity of AERONET observation sites in South America determined by correlation studies with MODIS aerosol optical depth. J. Geophys. Res. Atmos. 114, D21203. https://doi.org/10.1029/2008JD010369.

Hoffmann, C., Maglakelidze, M., von Schneidemesser, E., 2022. Asthma and COPD exacerbation in relation to outdoor air pollution in the metropolitan area of Berlin, Germany. Respir. Res. 23, 64. https://doi.org/10.1186/s12931-022-01983-1.

Huang, T., Li, Y., Li, J., Sung, J.J.Y., Yim, S.H.L., 2025. PM2.5-Associated premature mortality attributable to hot-and-polluted episodes and the inequality between the global north and the global south. GeoHealth 9. https://doi.org/10.1029/2024gh001290 e2024GH001290.

Ignotti, E., Hacon, S.D.S., Junger, W.L., Mourão, D., Longo, K., Freitas, S., Leon, A.C.M.P. D., 2010. Air pollution and hospital admissions for respiratory diseases in the subequatorial Amazon: a time series approach. Cad. Saude Publica 26, 747–761. https://doi.org/10.1590/S0102-311X2010000400017.

Instituto Brasileiro de Geografia e Estatística (IBGE), 2022. Cidades e Estados. https://www.ibge.gov.br/cidades-e-estados/ (acessado em 6 de junho de 2025).

Instituto Nacional de Meteorologia (INMET), 2022. Normais climatológicas do Brasil: período 1991–2020. Brasília: INMET. https://portal.inmet.gov.br/uploads/normais/NORMAISCLIMATOLOGICAS.pdf (acessado em 6 de junho de 2025).

Instituto Nacional de Pesquisas Espaciais (INPE), 2021. Programa queimadas. Monitoramento Dos Focos Ativos Por Estado. http://www.queimadas.dgi.inpe.br/queimadas/portal-static/estatisticas_estados/ (acessado em 9 de outubro de 2025).

Jaffe, D.A., Wigder, N.L., 2012. Ozone production from wildfires: a critical review. Atmos. Environ. 51, 1–10. https://doi.org/10.1016/j.atmosenv.2011.11.063.

Johnston, F.H., Henderson, S.B., Chen, Y., Randerson, J.T., Marlier, M., DeFries, R.S., Kinney, P., Bowman, D.M.J.S., Brauer, M., 2012. Estimated global mortality attributable to smoke from landscape fires. EHP Publishing 120 (5), 695–701. https://doi.org/10.1289/ehp.1104422.

Justice, C.O., et al., 2002. The MODIS fire products. Remote Sens. Environ. 83, 244–262. https://doi.org/10.1016/S0034-4257(02)00076-7.

Kelechi, A.H., Alsharif, M.H., Agbaetuo, C., Ubadike, O., Aligbe, A., Uthansakul, P., Kannadasan, R., Aly, A.A., 2022. Design of a low-cost air quality monitoring system using Arduino and ThingSpeak. Comput. Mater. Continua (CMC). https://doi.org/10.32604/cmc.2022.019431.

Koengkan, M., Fuinhas, J.A., Silva, N., 2021. Exploring the capacity of renewable energy consumption to reduce outdoor air pollution death rate in Latin America and the Caribbean region. Environ. Sci. Pollut. Res. 28, 1656–1674. https://doi.org/10.1007/s11356-020-10503-x.

Kumar, P., Morawska, L., Birmili, W., Paasonen, P., Hu, M., Kulmala, M., Harrison, R.M., Norford, L., Britter, R., 2014. Ultrafine particles in cities. Environ. Int. 66, 1–10. https://doi.org/10.1016/j.envint.2014.01.013.

Lelieveld, J., Pozzer, A., Pöschl, U., Fnais, M., Haines, A., Münzel, T., 2020. Loss of life expectancy from air pollution compared to other risk factors: a worldwide perspective. Cardiovasc. Res. 116 (11), 1910–1917. https://doi.org/10.1093/cvr/cvaa025.

Liang, K.-Y., Zeger, S.L., 1986. Longitudinal data analysis using generalized linear models. Biometrika, v. 73, p. 13-22, 1986. Disponível em: https://doi.org/10.1093/biomet/73.1.13.

Libonati, R., Pereira, J.M.C., Da Camara, C.C., Peres, L.F., Oom, D., Rodrigues, J.A., Santos, F.L.M., Trigo, R.M., Gouveia, C.M.P., Machado-Silva, F., Enrich-Prast, A., Silva, J.M.N., 2021. Twenty-first century droughts have not increasingly exacerbated fire season severity in the Brazilian Amazon. Sci. Rep. 11, 4400. https://doi.org/10.1038/s41598-021-82158-8.

Listyarini, S., Warlina, L., Sambas, A., 2021. Air quality monitoring system in South Tangerang based on Arduino Uno: from analysis to implementation. IOP Conf. Ser. Mater. Sci. Eng. 1115 (1), 012046. https://doi.org/10.1088/1757-899X/1115/1/012046.

Lita, I., Visan, D.A., Cioc, I.B., Mazare, A.G., Teodorescu, R.M., 2016. Indoor environmental parameters monitoring for building automation systems. In: 2016 8th International Conference on Electronics, Computers and Artificial Intelligence (ECAI), pp. 1–4. https://doi.org/10.1109/ECAI.2016.7861083.

Liu, N., Hao, Z., Zhao, P., 2024. Spatiotemporal change of PM2.5 concentration in beijing-tianjin-hebei and its prediction based on machine learning. Urban Clim. 58, 102167. https://doi.org/10.1016/j.uclim.2024.102167.

Machado-Silva, F., Libonati, R., Lima, T.F.M., Peixoto, R.B., França, J.R.A., Magalhães, M.A.F.M., 2020. Drought and fires influence the respiratory diseases hospitalizations in the amazon. Ecol. Indic. 109, 105817. https://doi.org/10.1016/j.ecolind.2019.105817.

Martin, S.T., Andreae, M.O., Artaxo, P., Baumgardner, D., Chen, Q., Goldstein, A.H., Guenther, A., Heald, C.L., Mayol-Bracero, O.L., McMurry, P.H., Pauliquevis, T., Pöschl, U., Prather, K.A., Roberts, G.C., Saleska, S.R., Dias, M.a.S., Spracklen, D.V., Swietlicki, E., Trebs, I., 2010. Sources and properties of Amazonian aerosol particles. Rev. Geophys. 48, RG2002. https://doi.org/10.1029/2008rg000280.

Martins, E.A., Gomes, A.C., Leitão, E., Almeida, D., Raiol, A., Batalha, S.S., Silva, G., Mandú, T., 2024. Análise do conforto térmico para os meses de abril e outubro da Vila de Alter do Chão, Santarém/PA. E&S Eng. Sci. 13 (4), 1–11. https://doi.org/10.18607/ES20241318404.

Martins, L.D., Hallak, R., Alves, R.C., de Almeida, D.S., Squizzato, R., Moreira, C.A., 2018. Long-range transport of aerosols from biomass burning over southeastern South America and their implications on air quality. Aerosol Air Qual. Res. 18, 1734–1745. https://doi.org/10.4209/aaqr.2017.11.0545.

Maung, T.Z., Bishop, J.E., Holt, E., Turner, A.M., Pfrang, C., 2022. Indoor air pollution and the health of vulnerable groups: a systematic review focused on particulate matter (PM), volatile organic compounds (VOCs) and their effects on children and people with pre-existing lung disease. Int. J. Environ. Res. Publ. Health 19 (14), 8752. https://doi.org/10.3390/ijerph19148752.

Monteiro dos Santos, D., de Oliveira, A.M., Duarte, E.S.F., et al., 2024. Compound dry-hot-fire events connecting Central and Southeastern South America: an unapparent and deadly ripple effect. Npj Nat. Hazards. 1, 32. https://doi.org/10.1038/s44304-024-00031-w.

Morawska, L., Thai, P.K., Liu, X., Asumadu-Sakyi, A., Ayoko, G., Bartonova, A., Bedini, A., Chai, F., Christensen, B., Dunbabin, M., Gao, J., Hagler, G.S.W., Jayaratne, R., Kumar, P., Lau, A.K.H., Louie, P.K.K., Mazaheri, M., Ning, Z., Motta, N., Mullins, B., Williams, R., 2018. Applications of low-cost sensing technologies for air quality monitoring and exposure assessment: how far have they gone? Environ. Int. 116, 286–299. https://doi.org/10.1016/j.envint.2018.04.018.

Moritz, M.A., Morais, M.E., Summerell, L.A., Carlson, J.M., Doyle, J., 2005. Wildfires, complexity, and highly optimized tolerance. Proc. Natl. Acad. Sci. 102, 17912–17917. https://doi.org/10.1073/pnas.0508985102.

Mullick, I.U., Faisal, K.A., Nishat, T.I., Bhuyan, M.H., 2024. Portable air quality detector using DSM501A dust sensor and Arduino Uno. J. Eng. Res. Rep. 26 (5), 163–174. https://doi.org/10.9734/jerr/2024/v26i51143.

NASA, 2023. Fire information for resource management system (FIRMS). NASA/LAADS/GSFC. https://firms.modaps.eosdis.nasa.gov (acessado em 1 de agosto de 2025).

Nawaz, M.O., Henze, D.K., 2020. Premature deaths in Brazil associated with long-term exposure to PM2.5 from Amazon fires between 2016 and 2019. GeoHealth 4. https://doi.org/10.1029/2020GH000268 e2020GH000268.

Oliveira, B.F.A., Ignotti, E., Hacon, S.S., 2012. A systematic review of the physical and chemical characteristics of pollutants from biomass burning and combustion of fossil fuels and health effects in Brazil. Cad. Saude Publica 28, 1675–1698. https://doi.org/10.1590/S0102-311X2012000900004.

Pan, W., 2001. Akaike's information criterion in generalized estimating equations. Biometrics 57, 120–125. https://doi.org/10.1111/j.0006-341x.2001.00120.x.

Peel, M.C., Finlayson, B.L., McMahon, T.A., 2007. Updated world map of the Köppen-Geiger climate classification. Hydrol. Earth Syst. Sci. 11, 1633–1644. https://doi.org/10.5194/hess-11-1633-2007.

Penza, M., 2020. Low-cost sensors for outdoor air quality monitoring. In: Advanced Nanomaterials for Inexpensive Gas Microsensors (Chapter 12). Elsevier. https://doi.org/10.1016/B978-0-12-814827-3.00012-8.

Pereira, B.B., Limongi, J.E., 2015. Epidemiologia de desfechos na saúde humana relacionados à poluição atmosférica no Brasil: uma revisão sistemática. Cad. Saúde Colet. (Rio J.) 23, 91–100. https://doi.org/10.1590/1414-462X201400050103.

Pereira, G.M., da Silva Caumo, S.E., Grandis, A., do Nascimento, E.Q.M., Correia, A.L., de Melo Jorge Barbosa, H., 2021. Physical and chemical characterization of the 2019 "black rain" event in the metropolitan area of São Paulo, Brazil. Atmos. Environ. 248, 118229. https://doi.org/10.1016/j.atmosenv.2021.118229.

Pöhlker, M.L., Pöhlker, C., Ditas, F., Klimach, T., De Angelis, I.H., Araújo, A., Brito, J., Carbone, S., Cheng, Y., Chi, X., Ditz, R., Gunthe, S.S., Kesselmeier, J., Könemann, T., Lavrič, J.V., Martin, S.T., Mikhailov, E., Moran-Zuloaga, D., Rose, D., Pöschl, U., 2016. Long-term observations of cloud condensation nuclei in the Amazon rain forest – part 1: aerosol size distribution, hygroscopicity, and new model parametrizations for CCN prediction. Atmos. Chem. Phys. 16, 15709–15740. https://doi.org/10.5194/acp-16-15709-2016.

Pozzer, A., Anenberg, S.C., Dey, S., Haines, A., Lelieveld, J., Chowdhury, S., 2023. Mortality attributable to ambient air pollution: a review of global estimates. GeoHealth 7. https://doi.org/10.1029/2022GH000711 e2022GH000711.

Priya, C.G., Pandu, M.A., Chandra, B., 2017. Automatic plant monitoring and controlling system over GSM using sensors. In: 2017 IEEE Technological Innovations in ICT for Agriculture and Rural Development (TIAR), pp. 173–176. https://doi.org/10.1109/TIAR.2017.8273710.

Reddington, C.L., Butt, E.W., Ridley, D.A., Artaxo, P., Morgan, W.T., Coe, H., Spracklen, D.V., 2015. Air quality and human health improvements from reductions in deforestation-related fire in Brazil. Nat. Geosci. 8, 768–771. https://doi.org/10.1038/ngeo2535.

Rentschler, J., Leonova, N., 2023. Global air pollution exposure and poverty. Nat. Commun. 14, 4432. https://doi.org/10.1038/s41467-023-39797-4.

Requia, W.J., Amini, H., Mukherjee, R., Gold, D.R., Schwartz, J.D., 2021. Health impacts of wildfire-related air pollution in Brazil: a nationwide study of more than 2 million hospital admissions between 2008 and 2018. Nat. Commun. 12, 6555. https://doi.org/10.1038/s41467-021-26822-7.

Robinson, A.L., Donahue, N.M., Shrivastava, M.K., Weitkamp, E.A., Sage, A.M., Grieshop, A.P., Lane, T.E., Pierce, J.R., Pandis, S.N., 2007. Rethinking organic aerosols: semivolatile emissions and photochemical aging. Science 315, 1259–1262. https://doi.org/10.1126/science.1133061.

Sakila, V.S., Manohar, S., Ebenezer, P.A., 2023. Ambient particulate matter monitoring system using SDS011 sensor utilizing machine learning approach and ambit of blockchain technology. Mater. Today Proc. https://doi.org/10.1016/j.matpr.2023.03.366.

Sant'Anna, A., Alencar, A., Pinheiro, B., Araújo, C., Vormittag, E., Wicher, H., Borges, K., Faria, M., Andrade, M.F., Porto, P., Artaxo, P., Rocha, R., Esturba, T., Simoni, W.F., 2021. O Estado Da Qualidade do Ar No Brasil (Working Paper). WRI Brasil. https://www.wribrasil.org.br/sites/default/files/wri-o-estado-da-_qualidade-do-ar-no-brasil.pdf. (Accessed 6 June 2025).

Sant'Anna, A.B., Alencar, A., Téllez-Chávez, L., Carvalho, A., Guimarães, A., Moutinho, P., 2020. O Ar É Insuportável: Os Impactos Das Queimadas Associadas Ao Desmatamento Da Amazônia Brasileira Na Saúde. Human Rights Watch. https://www.hrw.org/pt/report/2020/08/26/376135. (Accessed 6 June 2025).

Santos, D.M.D., De Oliveira, A.M., Duarte, E.S.F., Rodrigues, J.A., Menezes, L.S., Albuquerque, R., De O Roque, F., Peres, L.F., Hoelzemann, J.J., Libonati, R., 2024. Compound dry-hot-fire events connecting Central and Southeastern South America: an unapparent and deadly ripple effect. Npj Nat. Hazards. 1, e00031. https://doi.org/10.1038/s44304-024-00031-w.

Secretaria de Desenvolvimento Urbano e Obras Públicas (SEDOP), 2017. Estudo Da Delimitação Da Região Metropolitana De Santarém. Governo do Estado do Pará, Belém, PA. https://www.seop.pa.gov.br/sites/default/files/estudo_de_delimitacao_da_regiao_metropolitana_de_santarem_0.pdf (acessado em 11 de outubro de 2025).

Serviço Brasileiro de Apoio às Micro e Pequenas Empresas (SEBRAE), 2003. Plano estratégico de desenvolvimento turístico comunitário de Alter do Chão e Caranazal. SEBRAE Regional Santarém.

Silva, A.M.C., Moi, G.P., Mattos, I.E., Hacon, S.S., 2014. Low birth weight at term and the presence of fine particulate matter and carbon monoxide in the Brazilian Amazon: a population-based retrospective cohort study. BMC Pregnancy Childbirth 14, 309. https://doi.org/10.1186/1471-2393-14-309.

Silva, S.S., Melo, A.W.F., Silvestre, O., Duarte, A., Dantas, T., Valadares, P.H.S., Brown, F., 2021. Importância do monitoramento da qualidade do ar na Amazônia para a saúde pública e o meio ambiente: o caso do Estado do Acre, Brasil. https://doi.org/10.13140/RG.2.2.31288.21768.

Singh, K., Tripathi, D., 2021. Particulate matter and human health. In: Otsuki, T. (Ed.), Environmental Health. IntechOpen. https://doi.org/10.5772/intechopen.100550.

Song, X., Guo, X., Hu, X., 2023. Human exposure risk assessment for infectious diseases due to temperature and air pollution: an overview of reviews. Environ. Sci. Pollut. Res. 30, 88272–88280. https://doi.org/10.1007/s11356-023-28453-5.

Souza, A.A., Oviedo, A., Santos, T.M., 2020. Impactos Na Qualidade do Ar E Saúde Humana Relacionados Ao Desmatamento E Queimadas Na Amazônia Legal Brasileira. Instituto de Pesquisas Espaciais, São José dos Campos; Instituto Socioambiental, São Paulo. https://acervo.socioambiental.org/acervo/documentos/impactos-na-qualidade-do-ar-e-saude-humana-relacionados-ao-desmatamento-e (acessado em 11 de outubro de 2025).

Squizzato, R., Nogueira, T., Martins, L.D., Martins, J.A., Astolfo, R., Machado, C.B., 2021. Beyond megacities: tracking air pollution from urban areas and biomass burning in Brazil. npj Clim. Atmos. Sci. 4, 17. https://doi.org/10.1038/s41612-021-00173-y.

Sutanto, S.J., Vitolo, C., Napoli, C.D., D'Andrea, M., Henny, A.J., Lanen, Van, 2020. Heatwaves, droughts, and fires: exploring compound and cascading dry hazards at the Pan-European scale. Environ. Int. 134, 105276. https://doi.org/10.1016/j.envint.2019.105276.

Tran, H.M., Tsai, F.-J., Lee, Y.-L., Chang, J.-H., Chang, L.-T., Chang, T.-Y., Chung, K.F., Kuo, H.-P., Lee, K.-Y., Chuang, K.-J., Chuang, H.-C., 2023. The impact of air pollution on respiratory diseases in an era of climate change: a review of the current evidence. Sci. Total Environ. 898, 166340. https://doi.org/10.1016/j.scitotenv.2023.166340.

Tsai, S.-S., Chiu, Y.-W., Weng, Y.-H., Yang, C.-Y., 2022. Association between fine particulate air pollution and the risk of death from lung cancer in Taiwan. J. Toxicol. Environ. Health 85 (10), 431–438. https://doi.org/10.1080/15287394.2022.2040672.

Urbanski, S.P., Hao, W.M., Baker, S., 2008. Chapter 4 chemical composition of wildland fire emissions. In: Developments in Environmental Science. Elsevier, pp. 79–107. https://doi.org/10.1016/S1474-8177(08)00004-1.

Valente, F., Laurini, M., 2023. A spatio-temporal analysis of fire occurrence patterns in the Brazilian Amazon. Sci. Rep. 13, 12727. https://doi.org/10.1038/s41598-023-39875-z.

Vitolo, C., Napoli, C., Giuseppe, F., Cloke, H.L., Pappenberger, F., 2019. Mapping combined wildfire and heat stress hazards to improve evidence-based decision making. Environ. Int. 127, 21–34. https://doi.org/10.1016/j.envint.2019.03.008.

Vormittag, E.P.A., Cirqueira, S.S.R., Wicher Neto, H., Saldiva, P.H.N., 2021. Análise do monitoramento da qualidade do ar no Brasil. Estud. Avançados 35, 7–30. https://doi.org/10.1590/s0103-4014.2021.35102.002.

Wang, J., Krejci, R., Giangrande, S., Kuang, C., Barbosa, H.M.J., Brito, J., Carbone, S., Chi, X., Comstock, J., Ditas, F., Lavric, J., Manninen, H.E., Mei, F., Moran-Zuloaga, D., Pöhlker, C., Pöhlker, M.L., Saturno, J., Schmid, B., Souza, R.a.F., Martin, S.T., 2016. Amazon boundary layer aerosol concentration sustained by vertical transport during rainfall. Nature 539, 416–419. https://doi.org/10.1038/nature19819.

Wardoyo, A.Y.P., Dharmawan, H.A., Nurhuda, M., Adi, E.T.P., 2020. Optimization of PM2.5 Measurement system using NOVA SDS011 sensor. J. Phys., Conf. Ser. 1428, 012053. https://doi.org/10.1088/1742-6596/1428/1/012053.

World Health Organization, 2021. WHO Global Air Quality Guidelines: Particulate Matter (PM2.5 and PM10), Ozone, Nitrogen Dioxide, Sulfur Dioxide and Carbon Monoxide. World Health Organization. https://iris.who.int/handle/10665/345329. License: CC BY-NC-SA 3.0 IGO.

Ye, T., Xu, R., Yue, X., Chen, G., Yu, P., Coêlho, M.S.Z.S., Saldiva, P.H.N., Abramson, M. J., Guo, Y., Li, S., 2022. Short-term exposure to wildfire-related PM2.5 increases mortality risks and burdens in Brazil. Nat. Commun. 13, 7651. https://doi.org/10.1038/s41467-022-35326-x.

Zeger, S.L., Liang, K.Y., 1986. Longitudinal data analysis for discrete and continuous outcomes. Biometrics 42 (1), 121–130.

Zender-Swiercz, E., Galiszewska, B., Telejko, M., Starzomska, M., 2024. The effect of temperature and humidity of air on the concentration of particulate matter - PM2.5 and PM10. Atmos. Res. 312, 107733. https://doi.org/10.1016/j.atmosres.2024.107733.